1   • Full paper contribution

2   • XXX words in the main text, along with 8 tables and 15 figures

3   --

Numerical integration of an elasto-plastic critical state model for soils under unsaturated conditions

6   Author 1

7   • Martí Lloret-Cabot, Ph.D

8   Assistant Professor of Civil and Environmental Engineering

9   Department of Engineering

10   Durham University

11   UK

12   Author 2

13   • Simon J. Wheeler, Professor

14   Cormack Professor of Civil Engineering

15   James Watt School of Engineering

16   University of Glasgow

17   UK

18   Author 3

19   • Antonio Gens, Professor

20   Professor of Civil Engineering

21   Department of Civil and Environmental Engineering

22   Universitat Politècnica de Catalunya - CIMNE

23   Spain

24   Author 4

25   • Scott W. Sloan, Laureate Professor†

26   Professor of Civil Engineering

27   Priority Research Centre for Geotechnical Science and Engineering

28   The University of Newcastle

29   Australia.

30   †Laureate Professor Scott Sloan passed away unexpectedly during the preparation of this paper. The authors dedicate this work
31   to his memory

32

33   ABSTRACT

34   This paper presents the complete set of incremental equations for the numerical

35   integration of the Glasgow Coupled Model (GCM) and a comprehensive algorithm for

36   its numerical integration. The incremental formulation proposed is expressed in terms

37   of strain and suction increments (i.e. strain-driven) and defines an initial value problem

38   (IVP) that can be solved once the initial state and the pair of increments of the driven

39   variables are known. The numerical integration of this IVP is carried out by extending

40   to unsaturated condition, the well-known explicit substepping formulation with

41   automatic error control widely used for saturated soils. A notable feature of the

42   substepping integration scheme presented is that it integrates simultaneously the model

43   equations for both mechanical and water retention responses. Hence, the estimate of the

44   local truncation error to automatically adjust the size of the integration step is not only

45   affected by the local error in stresses and mechanical hardening parameter (as in a

46   saturated soil model) but, additionally, by the local error incurred in the integration of

47   the water retention relations (i.e. degree of saturation and water retention hardening

48   parameter). The correctness of the integration scheme is then verified by comparison

49   of computational outcomes against analytical/reference solutions.

50

51

52

1. INTRODUCTION

Advanced numerical methods have been applied to geomechanics during the last decades to solve geotechnical problems involving unsaturated soils (e.g. Pinyol et al., 2008, Borja and White, 2010, Cattaneo et al., 2014, Sheng et al., 2003ab, Gens, 2010, Khalili et al., 2008, Ng et al., 2000, Nuth and Laloui, 2008, Tsiampousi et al., 2013, Zhou and Sheng, 2015, Zhang et al., 2019). A key aspect in many of these numerical applications is the amount of water retained in the soil pores because it controls the loss or gain of soil's strength, critical to geotechnical instabilities. When the soil reaches full saturation after intense rainfall, for instance, all the additional contribution of the unsaturated condition to the soil strength vanishes. Changes in the saturation of the soil are also relevant to serviceability design because substantial volumetric compressions may occur during wetting (collapse) or drying (shrinkage) (Alonso et al., 1990, Gallipoli et al., 2003, Lloret-Cabot et al., 2014).

The amount of water stored within the pores of a soil is described by the water retention behaviour which relates the degree of saturation S_r (or the water content w) to matric suction s (where s is the difference between pore air pressure u_a and pore water pressure u_w). However, due to the occurrence of hysteresis, a one-to-one relation between S_r and s is rarely observed in soils (Romero et al., 1999, Tarantino 2009, Wheeler et al., 2003). In addition to this hysteresis, the water retention behaviour can be highly dependent on changes of the soil's porosity and, hence, on the mechanical behaviour (Romero et al., 1999, Tarantino 2009, Wheeler et al., 2003).

In order to represent accurately the potential changes in saturation when a soil is subjected to external environmental actions it is necessary to use a model that properly handles not only retention hysteresis but also the couplings between the mechanical behaviour and the water retention response. A model that includes all these effects is the Glasgow Coupled Model GCM (Wheeler et al., 2003; Lloret-Cabot et al., 2013), and the major focus of this paper is the development of an integration scheme capable to integrate, accurately and efficiently, the incremental constitutive relations of this model.

The explicit substepping formulation with automatic error control proposed in Sloan, (1987) and Sloan et al. (2001) has been extensively used in the literature for the numerical integration of elasto-plastic models for saturated soils (Sloan et al., 2001, Abbo, 1997, Sheng et al., 2000, Pedroso et al., 2008, Zhao et al., 2005, Pérez-Foguet et

al., 2001). Full extension of this formulation to the unsaturated case is presented in this paper in the context of the GCM. The extended substepping integration scheme integrates simultaneously the model equations for both mechanical and water retention responses. Hence, the local error incurred during the numerical integration of the model is not only affected by the local error in stresses and mechanical hardening parameters (as in the saturated case) but, additionally, by the local error incurred in the integration of the water retention relations. A consequence of this is that the measure of the local error used in a substepping integration scheme to adjust automatically the size of the next integration step is now estimated accounting for both sources of numerical error, including the inexact integration of the mechanical and water retention relations. Equivalent conclusions are reached when integrating other coupled constitutive models for unsaturated soils with substepping integration schemes with automatic error control (Zhang and Zhou, 2016).

The paper presents a comprehensive algorithm for the numerical integration of the GCM. Although some aspects of the algorithm are linked to specific features of the GCM, the overall approach is general and can be applied to other coupled constitutive models for unsaturated soils.

A small reformulation of the GCM is first presented with the aim of simplifying its numerical integration. Based on this reformulation, the relevant incremental mechanical and water retention relations of the model for each possible response, including unsaturated and saturated conditions, are developed. Two explicit substepping integration schemes with automatic error control are proposed in order to investigate the accuracy of the numerical integration: the second order modified Euler with substepping and the fifth order Runge-Kutta-Dormand-Prince with substepping. A verification study is presented at the end of the paper extending to unsaturated conditions, the verification strategy proposed in Lloret-Cabot et al. (2016) for saturated soils.

2. REFORMULATING GCM

Certain aspects of the GCM are reformulated in this section with the aim of simplifying its numerical integration. This reformulation does not involve any modification of the model, simply a change in how it is presented.

117 The version of the GCM presented here is that given in Lloret-Cabot et al. (2017), which

118 assumes that there are no elastic changes of degree of saturation (the gradient of elastic

119 scanning curves in the water retention plane is zero i.e. $\kappa_s = 0$ in the original model of

120 Wheeler et al., 2003), in order to achieve consistent behaviour across transitions

121 between unsaturated and saturated states.

122 Soil mechanics sign convention is adopted hereafter (compression positive). Vectors

123 and tensors are indicated in bold and the superscript T indicates transposed.

124 2.1. Mechanical Behaviour

125 The mechanical behaviour describes the stress-strain relations. In the GCM, strains are

126 related to the "Bishop's stress" tensor $\boldsymbol{\sigma}^*$, defined as:

127 $\quad \boldsymbol{\sigma}^* = \boldsymbol{\sigma} - \mathbf{m}^T \left(S_r u_w - (1 - S_r) u_a \right) = \overline{\boldsymbol{\sigma}} + \mathbf{m}^T S_r s$ \hfill (1)

128 where $\boldsymbol{\sigma}$ is the total stress tensor, $\mathbf{m}^T = (1,1,1,0,0,0)$ an auxiliary vector, S_r the degree

129 of saturation, u_a the pore air pressure, u_w the pore water pressure, s matric suction and

130 $\overline{\boldsymbol{\sigma}}$ net stress tensor ($\overline{\boldsymbol{\sigma}} = \boldsymbol{\sigma} - \mathbf{m}^T u_a$). Equation 1 reverts to the saturated effective stress

131 tensor $\boldsymbol{\sigma}'$ (i.e. $\boldsymbol{\sigma}' = \boldsymbol{\sigma} - \mathbf{m}^T u_w$) when $S_r = 1$.

132 *2.1.1 Elastic response*

133 The incremental elastic relationship between Bishop's stress and strains is given by:

134 $\quad d\boldsymbol{\sigma}^* = \mathbf{D}_e d\boldsymbol{\varepsilon}$ \hfill (2)

135 where d refers to an infinitesimal variation and $\mathbf{D}_e$ is the elastic stiffness matrix:

136 $$\mathbf{D}_e = \begin{pmatrix} K + \frac{4}{3}G & K - \frac{2}{3}G & K - \frac{2}{3}G & 0 & 0 & 0 \\ & K + \frac{4}{3}G & K - \frac{2}{3}G & 0 & 0 & 0 \\ & & K + \frac{4}{3}G & 0 & 0 & 0 \\ symmetric & & & G & 0 & 0 \\ & & & & G & 0 \\ & & & & & G \end{pmatrix} \quad (3)$$

137 K and G in Equation 3 are, respectively, the elastic tangential bulk and shear moduli

138 defined as:

5

139 $$K = \frac{\mathrm{d}p^*}{\mathrm{d}\varepsilon_v^e} = \frac{vp^*}{\kappa} \qquad (4)$$

140 $$G = \frac{\mathrm{d}q}{3\mathrm{d}\varepsilon_d^e} \qquad (5)$$

141 where p^* is the mean Bishop's stress, q is the deviatoric stress, ε_v^e is the elastic

142 volumetric strain, ε_d^e is the elastic deviatoric strain, v is the specific volume and κ is

143 the gradient of a swelling line in the $v{:}\ln p^*$ plane. A variety of expressions are possible

144 for G (Potts and Zdravkovic, 1999), but the simplest is to assume a constant value of

145 shear modulus.

146 Given that $\boldsymbol{\sigma}^* = \boldsymbol{\sigma}'$ when $S_r = 1$, Equation 2 has the advantage of converging naturally

147 to the conventional saturated elastic relations of the Modified Cam Clay model, MCC

148 (Roscoe and Burland, 1968).

149 *2.1.2. Mechanical yield curve*

150 In order to reduce potential inaccuracies in the evaluation of the mechanical yield curve

151 f_M, Sheng et al. (2000) propose that f_M is normalised against a stress parameter, so that

152 its evaluation is not significantly influenced by the magnitude of stresses. Using the

153 preconsolidation stress p^*_0 (also referred to as the mechanical yield stress) as a

154 normalising factor, the general expression for the mechanical yield curve of the GCM

155 is (Lloret-Cabot et al., 2013):

156 $$f_M = \frac{3J_2}{\left(p^*_0\right)^2} + M(\theta)^2 \left[\left(\frac{p^*}{p^*_0}\right)^2 - \frac{p^*}{p^*_0} \right] = 0 \qquad (6)$$

157 where J_2 is the second invariant of the deviatoric stress tensor $\mathbf{s}$ (i.e. $\mathbf{s} = \boldsymbol{\sigma}^* - \mathbf{m}^T p^*$) and

158 $M(\theta)$ is a function of the Lode's angle θ describing the shape of the mechanical yield

159 surface in the deviatoric plane (Potts and Gens, 1984). Available expressions for $M(\theta)$

160 in the literature for saturated conditions (e.g. Potts and Gens, 1984, Potts and

161 Zdravkovic, 1999, Sheng et al., 2000) can be readily incorporated to the unsaturated

162 case. However, for simplicity, M is assumed constant herein. Then, for axisymmetric

163 conditions, the mechanical yield curve becomes:

164 $$f_M = \frac{q^2}{\left(p^*_0\right)^2} + M^2 \left[\left(\frac{p^*}{p^*_0}\right)^2 - \frac{p^*}{p^*_0} \right] = 0 \qquad (7)$$

165 where M is the slope of the critical state line in the q:p^* plane and q is the deviatoric

166 stress i.e. $q^2 = 3J_2$.

167 Expressions for M(θ) are possible by extending to the unsaturated case available

168 expressions in the literature for saturated conditions (e.g. Potts and Gens, 1984, Potts

169 and Zdravkovic, 1999, Sheng et al., 2000). For simplicity, axisymmetric conditions are

170 assumed in the formulation presented here, so that M can be assumed a soil constant.

171 The preconsolidation stress p^*_0 varies with the degree of saturation S_r according to:

172 $$p^*_0 = p'_0 \exp\left(\frac{k_1}{\lambda_s}(1-S_r)\right) \qquad (8)$$

173 where p'_0 is the value of the saturated preconsolidation stress. k_1 and λ_s are soil

174 constants.

175 Equation 6 indicates that the mechanical yield curve f_M is elliptical in shape (of aspect

176 ratio M) when plotted in the q:p^* plane (Figure 1). The size of this ellipse is defined by

177 the current value of mechanical yield stress p^*_0, and this varies linearly with the degree

178 of saturation in the S_r: $\ln p^*$ plane (Equation 8). For the special case of $S_r = 1$, the

179 mechanical yield curve corresponds to the conventional ellipse of the MCC (Figure 1),

180 because $p^*_0 = p'_0$, which simplifies the implementation of the GCM in finite element

181 programs where the MCC is already available.
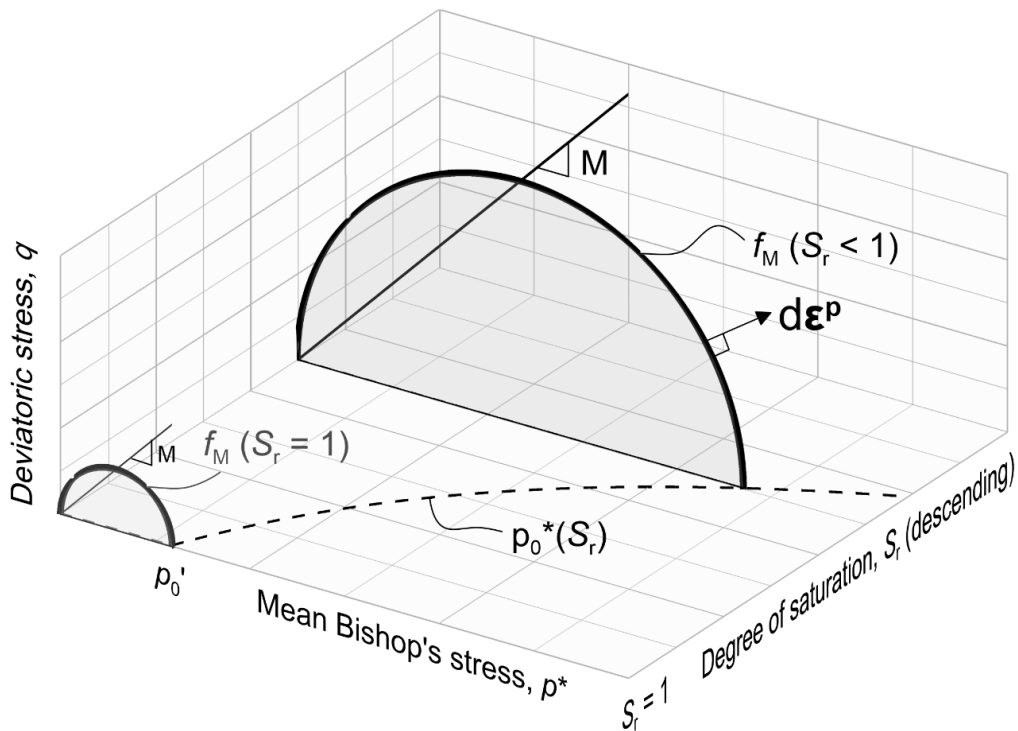
182

183 Figure 1 Typical mechanical yield curves of the GCM for a general value of S_r and for

184 $S_r = 1$ in the p^*:q:S_r space.

185   Interestingly, the new form of expressing the variations of mechanical yield stress with

186   degree of saturation given by Equation 8 resembles the expression proposed by Jommi

187   and Di Prisco (1994), with the difference here that the GCM represents the variation of

188   degree of saturation within a single constitutive framework. Some of the advantages in

189   constitutive modelling of expressing the mechanical (Bishop's) yield stress p^{*}_{0} in terms

190   of degree of saturation are discussed in Lloret-Cabot & Wheeler (2018). Also, when

191   the mechanical yield condition in GCM is represented in terms of Bishop's stresses and

192   degree of saturation (as in Figure 1), there is no movement of the yield surface until the

193   soil state reaches the surface. This contrasts with the original presentation of the GCM

194   in Wheeler et al. (2003), where coupled movements of the mechanical yield surface

195   (expressed there in terms of Bishop's stresses and modified suction s^{*} (defined later))

196   occur during yielding on water retention yield surfaces. As a consequence, the new

197   formulation has advantages in numerical modelling. Firstly, it is easier to use various

198   common numerical techniques that have been developed to overcome issues arising

199   when performing explicit numerical integration of saturated elasto-plastic critical state

200   models (e.g. yield intersection, elasto-plastic unloading, drift correction, etc). Secondly,

201   as demonstrated later, this specific form of f_{M} facilitates the formulation of an

202   unambiguous strategy to identify the correct model response activated by any given

203   stress path. Finally, it provides a very simple representation of the transitions between

204   saturated and unsaturated conditions that avoids the drawbacks discussed in Pedroso et

205   al. (2008) about the non-convex form of the mechanical yield curve at the transition

206   from unsaturated to saturated states.

207   *2.1.3. Hardening law*

208   Given that the saturated preconsolidation stress p'_{0} remains constant unless mechanical

209   yielding occurs, it is possible to relate p'_{0} to changes of plastic volumetric strains $d\varepsilon^{p}_{v}$

210   through the following hardening law:

211
$$\frac{dp'_{0}}{p'_{0}} = \frac{v}{\lambda - \kappa} d\varepsilon^{p}_{v} \qquad (9)$$

212   where κ is the gradient of a swelling line (in the v:ln p' plane for saturated conditions

213   and the v:ln p^{*} plane for unsaturated conditions) and λ is the gradient of the saturated

214   normal compression line in the v:ln p' plane.

215   Equation 9 is valid whether the soil is under saturated or unsaturated conditions and, as
216   in the Barcelona Basic Model of Alonso et al. (1990), p'_0 can be viewed in the GCM as
217   the mechanical hardening parameter. Equation 9 is identical to the conventional
218   volumetric hardening law of the MCC which, as highlighted earlier, is helpful when
219   combining existing critical state finite element formulations for saturated soils with the
220   GCM.

221   *2.1.4. Flow rule*

222   An associated flow rule is adopted for the mechanical behaviour:

223   $$d\boldsymbol{\varepsilon}^{\mathbf{p}} = d\lambda_{\mathrm{M}} \frac{\partial f_{\mathrm{M}}}{\partial \boldsymbol{\sigma}^{*}} \tag{10}$$

224   where $d\lambda_{\mathrm{M}}$ is an unknown positive scalar (referred to as the mechanical plastic
225   multiplier) to be found by imposing that the stress point remains on f_{M} during
226   mechanical yielding (consistency condition).

227   *2.1.5. Analytical relations for the mechanical behaviour*

228   The relationships for the mechanical behaviour of the GCM just presented lead to the
229   following analytical expressions for isotropic normal compression states and critical
230   states. These analytical expressions are relevant for verification purposes and provide
231   further insight on specific features of the GCM. For example, isotropic stress states
232   involving yielding on f_{M} are predicted to lie on a normal compression line in the v:lnp^{*}
233   plane, the position of which depends on the current value of S_r (see also Lloret-Cabot
234   et al. 2018ab):

235   $$v = \mathrm{N}(S_r) - \lambda \ln p^{*} \tag{11}$$

236   where

237   $$\mathrm{N}(S_r) = \mathrm{N} + \frac{k_1(\lambda - \kappa)(1 - S_r)}{\lambda_s} \tag{12}$$

238   and N is the intercept of the conventional saturated normal compression line (see Figure
239   2).

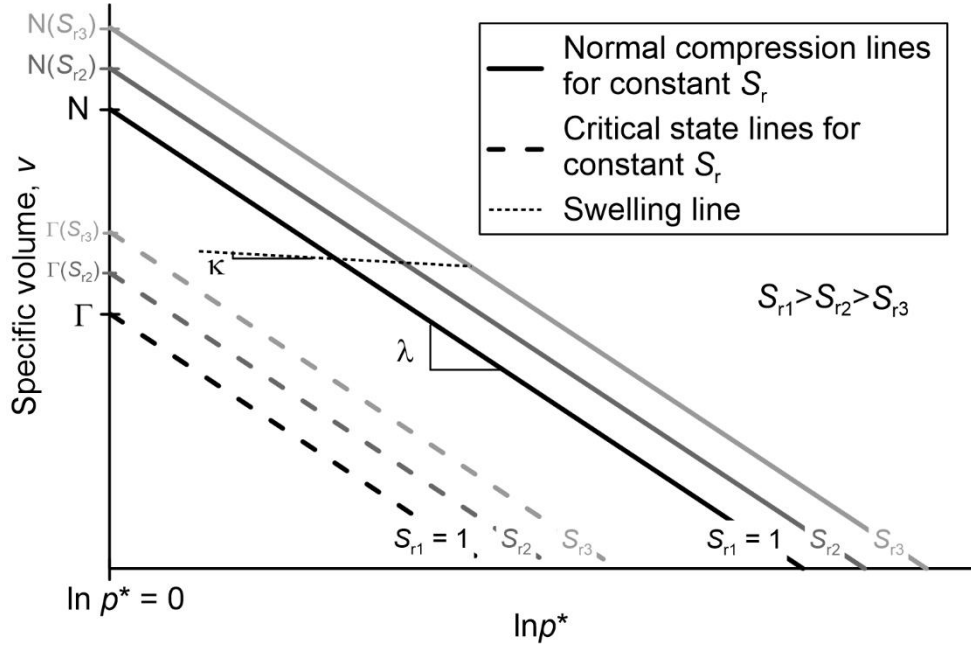240   Critical states, on the other hand, are defined by:

241   $$q = \mathrm{M}p^{*} \tag{13}$$

242   $$v = \Gamma(S_r) - \lambda \ln p^{*} \tag{14}$$

243 where q is the deviatoric stress and

244 $$\Gamma(S_r) = N(S_r) - (\lambda - \kappa)\ln 2 = \Gamma + \frac{k_1(\lambda - \kappa)(1 - S_r)}{\lambda_s} \qquad (15)$$

245 and Γ is the intercept of the conventional saturated critical state line (see Figure 2).

247 Figure 2. Normal compression and critical state lines for constant values of S_r in the
248 v:$\ln p^*$ plane.

249 2.2. Water Retention Behaviour

250 Water retention behaviour is typically expressed in terms of degree of saturation S_r and
251 matric suction s, however, based on the work of Houlsby (1997), the GCM relates S_r to
252 the "modified suction" s^*, defined as:

253 $$s^* = n(u_a - u_w) = \frac{v-1}{v}s \qquad (16)$$

254 where n is porosity.

255 *2.2.1. Elastic response*

256 For situations where the GCM is to be used for both unsaturated and saturated
257 conditions, Lloret-Cabot et al. (2017) recommends to assume that elastic variations of
258 degree of saturation are zero $dS_r^e = 0$ (the gradient in the original model of Wheeler et

10

259   al. (2003) of elastic scanning curves in the S_r:$\ln s^*$ plane is zero i.e. $\kappa_s = 0$). The same

260   assumption is made here.

2.2.2. Retention yield curves

262   Water retention behaviour is described by two yield functions: the wetting retention

263   yield curve f_{WR} and the drying retention yield curve f_{DR}. Variations of modified suction

264   occurring inside f_{WR} and f_{DR} result in no changes of S_r (i.e. $dS_r = dS_r^e = 0$). Yielding on

265   f_{WR} produces plastic increases of S_r (i.e. $dS_r = dS_r^p > 0$), whereas yielding on f_{DR} causes

266   plastic decreases of S_r (i.e. $dS_r = dS_r^p < 0$). Similarly to the mechanical yield curve, the

267   expression of the wetting retention yield curve is also normalised:

268    $$f_{WR} = \frac{s_1^* - s^*}{s_1^*} = 0 \tag{17}$$

269   where s_1^* is the wetting yield stress controlling the occurrence of yielding on f_{WR}

270   (equivalent to p_0^* for mechanical yielding).

271   The wetting yield stress s_1^* varies with the occurrence of mechanical yielding according

272   to:

273    $$s_1^* = s_{10}^* \left(\frac{p'_0}{p'_{00}} \right)^{k_2} = s_{10}^* \exp\left(\frac{-k_2}{\lambda - \kappa} \Delta v^p \right) \tag{18}$$

274   where k_2 is a coupling parameter, p'_0 is the mechanical hardening parameter and Δv^p

275   indicates plastic decreases of specific volume from a reference state. s_{10}^* and p'_{00} are,

276   respectively, the values of s_1^* and p'_0 at the reference states when $\Delta v^p = 0$.

277   Similarly, the expression of the drying retention yield curve is:

278    $$f_{DR} = \frac{s^* - s_2^*}{s_2^*} = 0 \tag{19}$$

279   where s_2^* is the drying yield stress for f_{DR} which varies with p'_0 (or Δv^p) according to:

280    $$s_2^* = s_{20}^* \left(\frac{p'_0}{p'_{00}} \right)^{k_2} = s_{20}^* \exp\left(\frac{-k_2}{\lambda - \kappa} \Delta v^p \right) \tag{20}$$

281   where s_{20}^* and p'_{00} are, respectively, the values of s_2^* and p'_0 when $\Delta v^p = 0$.

282   Equations 17 and 19 indicate, respectively, that the wetting retention yield curves f_{WR}

283   and the drying retention yield curve f_{DR} form two parallel straight lines when plotted in

284   the $\ln s^*$:$\ln p_0'$ plane (see Figure 3). The positions of these straight lines and their gradient

285   with respect to $\ln p_0'$ are given by Equations 18 and 20. The current values of the

286 parameters s_{10}^* and s_{20}^* (which correspond, respectively, to the values of s_1^* and s_2^* at

287 a reference state in which $p'_0 = p'_{00}$) fix the position of f_{WR} and f_{DR} respectively, whereas

288 the gradient is given by the value of the soil parameter k_2. Therefore, the parameters

289 s_{10}^* and s_{20}^* are equivalent to the mechanical hardening parameter p_0' and, hence, can

290 be viewed as the hardening parameters of the water retention response. Equations 17-

291 20 are still active under fully saturated conditions, because they track the influence of

292 mechanical yielding on the potential occurrence of desaturation on drying (i.e. air-entry

293 point) and re-saturation on wetting or loading (i.e. air-exclusion point).

294 The spacing between f_{WR} and f_{DR} is assumed constant when plotted in terms of $\ln s^*$ (i.e.

295 $s_2^* = R \cdot s_1^*$, where R is a soil constant (Lloret-Cabot et al., 2017) and this spacing defines

296 the current range of values of s^* for which no plastic changes of S_r will occur at a given

297 value of p'_0. Hence, the spacing between f_{WR} and f_{DR} in the $\ln s^*:\ln p_0'$ plane defines the

298 elastic domain of the water retention behaviour (see shaded zone in Figure 3). Yielding

299 on the drying retention yield curve reduces the values of S_r and causes a coupled

300 movement of the wetting retention yield curve (Wheeler et al., 2003). Equivalent

301 comments apply when yielding on f_{WR}.
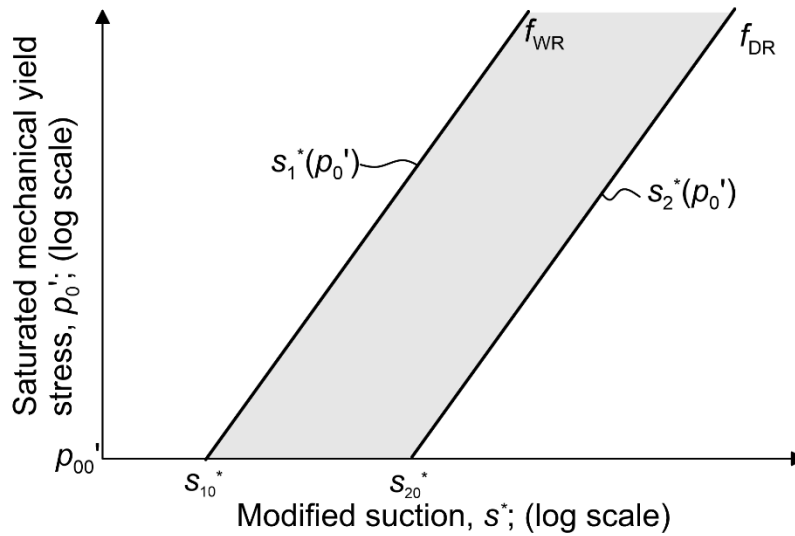
302

303 Figure 3. Water retention yield curves in $\ln s^*:\ln p_0'$ plane.

304 *2.2.3. Hardening law*

305 Given that s_{10}^* and s_{20}^* remain constant unless water retention yielding occurs, it is

306 possible to relate them to plastic changes of degree of saturation $\mathrm{d}S_r^p$ through the

307 following hardening law:

308 $$\frac{\mathrm{d}s_{10}^{*}}{s_{10}^{*}} = \frac{\mathrm{d}s_{20}^{*}}{s_{20}^{*}} = \frac{-\mathrm{d}S_{r}^{p}}{\lambda_{s}} \qquad (21)$$

309 where λ_{s} is the gradient of a main wetting/drying curve in the S_{r}:lns^{*} plane.

310 For completeness, it is useful to include here how the water retention yield stress s_{R}^{*}

311 (where the subscript R is 1 for f_{WR} and 2 for f_{DR}) vary against the water retention and

312 mechanical hardening parameters:

313 $$\frac{\mathrm{d}s_{R}^{*}}{s_{R}^{*}} = \frac{\mathrm{d}s_{R0}^{*}}{s_{R0}^{*}} + k_{2}\frac{\mathrm{d}p'_{0}}{p'_{0}} \qquad (22)$$

314 Similarly, the mechanical yield stress p_{0}^{*} varies with the mechanical and water retention

315 hardening parameters according to:

316 $$\frac{\mathrm{d}p_{0}^{*}}{p_{0}^{*}} = \frac{\mathrm{d}p'_{0}}{p'_{0}} + k_{1}\frac{\mathrm{d}s_{R0}^{*}}{s_{R0}^{*}} \qquad (23)$$

317 *2.2.4. Flow rule*

318 Associated flow rules are assumed for the water retention response:

319 $$\mathrm{d}S_{r}^{p} = \mathrm{d}S_{r} = -\mathrm{d}\lambda_{R}\frac{\partial f_{R}}{\partial s^{*}} \qquad (24)$$

320 where $\mathrm{d}\lambda_{R}$ is an unknown positive scalar (referred to as the water retention plastic

321 multiplier) to be found by imposing that the stress point remains on f_{R} during retention

322 yielding (consistency condition).

323 Given that $\mathrm{d}S_{r}^{e} = 0$ (Figure 4), total and plastic variations of S_{r} are the same ($\mathrm{d}S_{r} = \mathrm{d}S_{r}^{p}$

324).

325 *2.2.5. Analytical relations for the water retention behaviour*

326 The water retention relations just presented result in the following expressions for main

327 wetting and drying curves:

328 $$S_{r} = 1 - \lambda_{s}\ln\left(\frac{s^{*}}{s_{ex}^{*}}\right) \qquad (25)$$

329 $$S_{r} = 1 - \lambda_{s}\ln\left(\frac{s^{*}}{s_{e}^{*}}\right) \qquad (26)$$

330 where s_{ex}^{*} and s_{e}^{*} are, respectively, the current air-exclusion and air-entry values of

331 modified suction (see Figure 4). These air-exclusion and air-entry values of modified

13

332   suction are related to the saturated preconsolidation stress p_0' through the saturation and

333   desaturation lines, respectively (Lloret-Cabot et al., 2017):

334 $$\ln s_{ex}^* = \frac{\left(\Omega^* - 1\right)}{\lambda_s^*} + k_2 \ln p_0' \tag{27}$$

335    $$\ln s_e^* = \frac{\left(\Omega^* - 1\right)}{\lambda_s^*} + k_2 \ln p_0' + \ln R \tag{28}$$

336   where λ_s^* and Ω^* are soil constants corresponding to the gradient and intercept,

337   respectively, of the unsaturated normal compression planar surface for S_r derived in

338   Lloret-Cabot et al. (2017). λ_s^* can be expressed in terms of soil constants λ_s, k_1 and k_2

339   and Ω^* can be expressed in terms of soil constants N, N^*, λ, κ, λ_s and k_1 (see Appendix

340   A), where N^* is the intercept of the unsaturated normal compression planar surface for

341   v derived in Lloret-Cabot et al. (2017).

342   Combining main wetting and main drying equations with the saturation and

343   desaturation lines, respectively, the expressions of the main wetting and main drying

344   curves can be expressed in terms of p_0':

345    $$S_r = 1 + \left[\left(\Omega^* - 1\right)\left(1 - k_1 k_2\right) + k_2 \lambda_s \ln p_0'\right] - \lambda_s \ln s^* \tag{29}$$

346    $$S_r = 1 + \left[\lambda_s \ln R + \left(\Omega^* - 1\right)\left(1 - k_1 k_2\right) + k_2 \lambda_s \ln p_0'\right] - \lambda_s \ln s^* \tag{30}$$
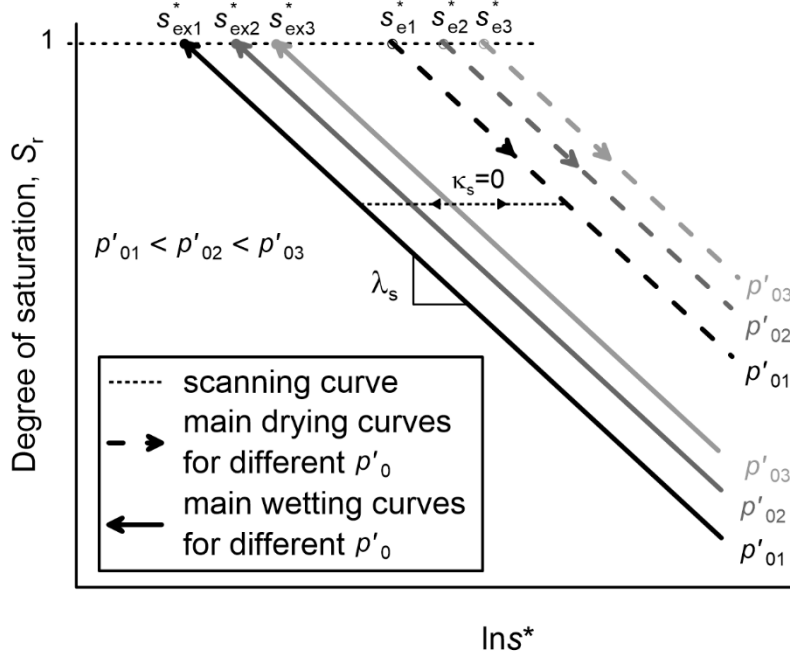
347

348   Figure 4. Main wetting and main drying water retention curves for constant values of

349   p_0' in the S_r:lns^* plane.

14

350   2.3. Model responses

351   There are six possible responses in the GCM to represent mechanical and water

352   retention behaviour of soils under saturated and unsaturated conditions. Each of them

353   is identified hereafter by an integer number assigned to the variable "STRPTH":

354   (1) STRPTH=1 is for purely elastic behaviour ($\Delta \boldsymbol{\varepsilon^p} = \mathbf{0}$ and $\Delta S_r = 0$).

355   (2) STRPTH=2 is for yielding on only f_{WR} ($\Delta \boldsymbol{\varepsilon^p} = \mathbf{0}$ and $\Delta S_r > 0$).

356   (3) STRPTH=3 is for yielding on only f_{DR} ($\Delta \boldsymbol{\varepsilon^p} = \mathbf{0}$ and $\Delta S_r < 0$).

357   (4) STRPTH=4 is for yielding on only f_M ($\Delta \boldsymbol{\varepsilon^p} \neq \mathbf{0}$ and $\Delta S_r = 0$).

358   (5) STRPTH=5 is for simultaneous yielding on f_M and f_{WR} ($\Delta \boldsymbol{\varepsilon^p} \neq \mathbf{0}$ and $\Delta S_r > 0$).

359   (6) STRPTH=6 for simultaneous yielding on f_M and f_{DR} ($\Delta \boldsymbol{\varepsilon^p} \neq \mathbf{0}$ and $\Delta S_r < 0$).

360   Transitions from unsaturated to saturated conditions (saturation) occur whilst on f_{WR}.

361   This means that an initially unsaturated soil ($S_r < 1$) can only saturate during stress paths

362   that involve yielding on f_{WR} (i.e. STRPTH=2 or STRPTH=5). Once the soil is saturated,

363   further increases of S_r are prevented (i.e. flow rule no longer applies on f_{WR}) and the

364   consistency condition on f_{WR} is removed so that the stress point can pass beyond f_{WR}

365   (see Lloret-Cabot et al., 2017, Lloret-Cabot et al., 2018ab for details).Transitions in the

366   reverse direction (desaturation), occur whilst on f_{DR}. In this case, an initially saturated

367   soil ($S_r = 1$) can only desaturate during stress paths that involve yielding on f_{DR} (i.e.

368   STRPTH=3 or STRPTH=6).

369   Typical examples of the six possible responses in the GCM are illustrated in Figure 5

370   for unsaturated states. Each response is represented by a pair of plots. The top plot

371   shows the water retention behaviour in the $\ln p_0':\ln s^*$ plane and the bottom one, the

372   mechanical response in the $S_r:\ln p^*$ plane. The initial position of each yield curve is

373   indicated by a solid line whereas, if yielding occurs, the corresponding final positions

374   of the yield curves are indicated by chain-dotted lines. Arrows indicate the movement

375   of the stress point and the shaded zone indicates other possible positions of the final

376   stress point that would also activate the same type of model response. For clarity, the

377   responses are shown for isotropic stress conditions, but equivalent conclusions apply in

378   general stress space.

379   Figure 5a shows an example of purely elastic behaviour (STRPTH=1) and corresponds

380   to a situation where the final stress point remains inside the elastic domain (i.e. $f_{WR} \leq$

381   *FTOL* & $f_{DR} \leq FTOL$ & $f_M \leq FTOL$, where *FTOL* is a specified tolerance) so that all

382   yield curves remain at the same initial position. In contrast, Figures 5b and 5c show

383   typical responses for retention yielding alone (STRPTH=2 or 3) causing plastic changes

384   of S_r. Note that in each of these two cases the retention curve not being yielded has also

385   moved from its initial position as a consequence of the associated movement defined

386   by Equation 21. No plastic straining occurs when STRPTH=2 or 3 because the stress

387   path remains inside f_M (Figures 5b and5c). As a consequence, the saturated mechanical

388   yield stress p_0' remains unchanged (and, hence, the mechanical yield curve does not

389   move).

390   Figure 5d shows an example of yielding on only f_M (STRPTH=4) where only the

391   mechanical yield curve moves from its initial position as a consequence of plastic

392   straining. Examples of yielding on two yield curves simultaneously are illustrated in

393   Figures 5e and 5f. In these, plastic straining and plastic changes of S_r occur at the same

394   time and, as a result, all yield curves move.

395   The forms of Equation 8 (for the mechanical response) and Equations 18 and 20 (for

396   water retention response) plotted in Figure 5 demonstrate one of the computational

397   advantages of the reformulated equations of the GCM discussed earlier. Equation 8, for

398   example, corresponds to the integrated form of how the coupling of the water retention

399   behaviour on the mechanical response is represented within the GCM. Similarly,

400   Equations 18 and 20, correspond to the integrated form of the coupling of the

401   mechanical response on the water retention. As further demonstrated later, these

402   integrated forms of the couplings between mechanical and retention responses facilitate

403   the identification of the active model response and simplify the intersection problem

404   arising when a stress path crosses a yield curve of the model.
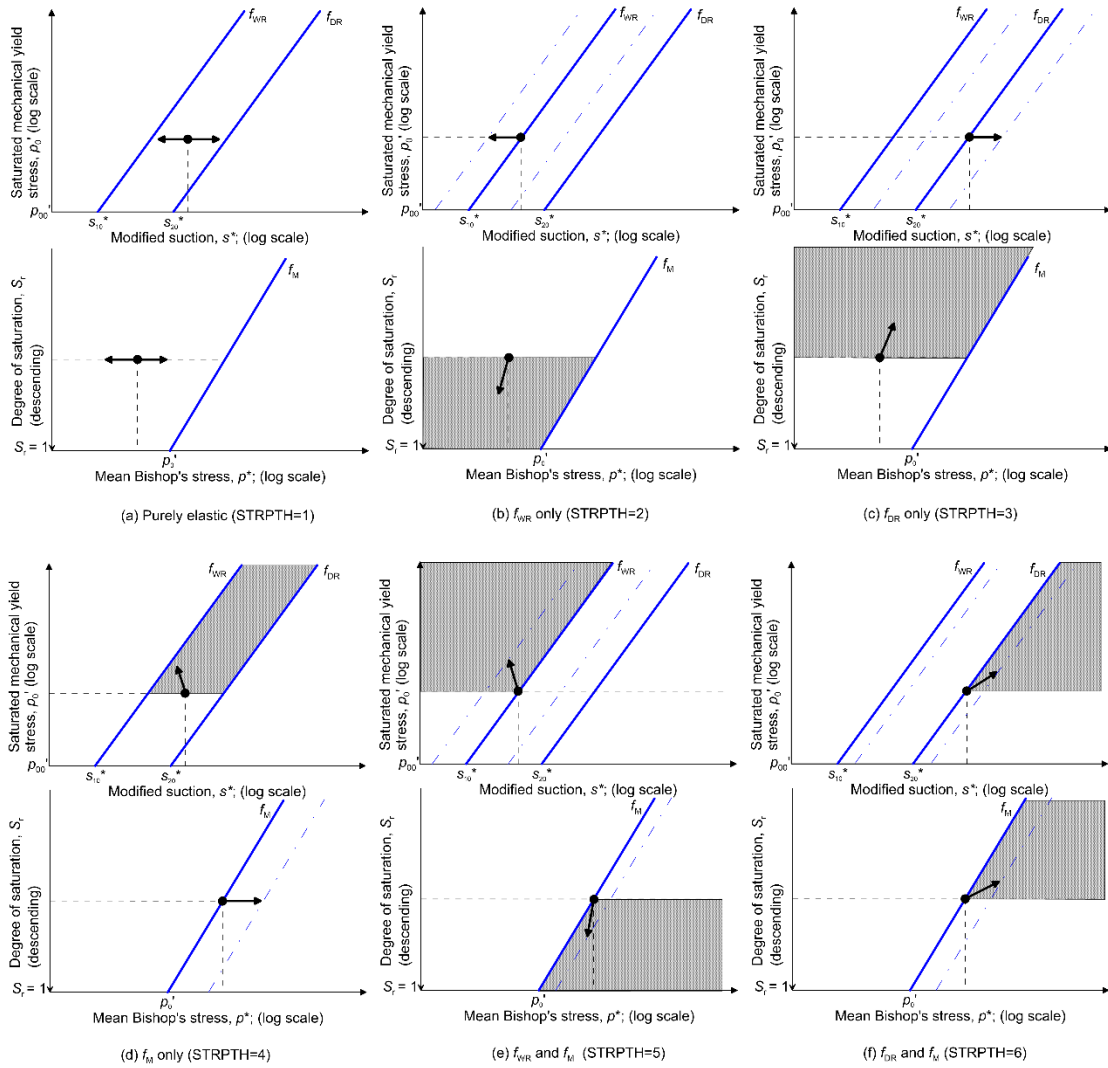
Figure 5 Typical model responses for isotropic stress states under unsaturated conditions.

3. MECHANICAL AND WATER RETENTION RELATIONS

When using the finite element method in problems involving saturated soils that may eventually desaturate, the *local* (i.e. within the element) integration of the coupled constitutive model representing the material behaviour of the soil involves the solution of both the mechanical and water retention incremental relations. During a typical finite element iteration in such problems, the nodal displacement and pore fluid pressures (including water and air) increments are usually found from the solution of the discretized *global* system of equations, typically involving equilibrium and mass balance relations (e.g. Olivella et al., 1996). Nodal displacement increments are combined with the strain-displacement relations to find the corresponding strain increments at a finite number of Gauss points within each element and, similarly, nodal

419   pore fluid pressures increments are combined to find the corresponding increment of

420   suction at each Gauss point. The known strain and suction increments can be then used

421   at the local level to find the corresponding increments of stresses and degree of

422   saturation via integration of the coupled constitutive model. It is hence convenient in

423   finite element analysis (FEA) to express the local integration algorithm in terms of the

424   *known* strain and suction increments (i.e. strain-driven algorithm). Because of their

425   compatibility in FEA, this section focuses on strain-driven formulations to integrate the

426   constitutive relations of the GCM, extending to unsaturated conditions the work on

427   explicit substepping algorithms with automatic error control proposed in Sloan et al.

428   (2001) for saturated soils.

429   3.1. Formulation of the problem

430   The numerical integration of a constitutive model for unsaturated soils involves the

431   solution of an initial value problem (IVP) defined by the incremental relationships of

432   the model, the initial (or current) state, the corresponding parameters of the model and,

433   in the context of strain-driven formulations, a given pair of $\Delta \boldsymbol{\varepsilon}$ and Δs (Δ denotes a finite

434   variation). Expressing the relations of the GCM by means of a strain-driven formulation

435   is very convenient because, irrespective of the model response active, Δs^* can be

436   computed correctly from the initial (or current) state at i and the exact updates of

437   specific volume v and matric suction s at $i+1$:

438   $$^{i+1}s = {}^{i}s + \Delta s \tag{31}$$

439   $$^{i+1}v = {}^{i}v \exp\left(-\Delta \varepsilon_{\mathrm{v}}\right) \tag{32}$$

440   The correct update of s^* at $i+1$ is then given by:

441   $$^{i+1}s^* = {}^{i+1}s \frac{{}^{i+1}v - 1}{{}^{i+1}v} \tag{33}$$

442   From where the correct increment of modified suction can be calculated:

443   $$\Delta s^* = {}^{i+1}s^* - {}^{i}s^* \tag{34}$$

444   Once the increments of modified suction are known, the remaining incremental

445   quantities can be expressed in a general IVP form as follows. The first two equations

446   describe the mechanical response (Bishop's stress – strain relations) and the second pair

447   the water retention response (modified suction – degree of saturation relations):

448   $$\Delta \boldsymbol{\sigma}^* = \mathbf{D}_e \Delta \boldsymbol{\varepsilon} - \Delta \lambda_{\mathrm{M}} \mathbf{D}_e \mathbf{a}_{\mathrm{M}} \tag{35}$$

$$449 \quad \Delta p_0' = \Delta\lambda_M B_M \tag{36}$$

$$450 \quad \Delta S_r = -\Delta\lambda_R a_R \tag{37}$$

$$451 \quad \Delta s_{R0}^* = -\Delta\lambda_R B_R \tag{38}$$

452 where the subscript M indicates mechanical response and the subscript R indicates

453 retention response (with 1 for f_{WR} and 2 for f_{DR}), $\Delta\lambda_M$ and $\Delta\lambda_R$ are the respective plastic

454 multipliers, p_0' and s_{R0}^* are the respective hardening parameters, $\mathbf{a_M}$ is the gradient of

455 the mechanical yield curve with respect to Bishop's stress, a_R is the derivative of the

456 retention yield curve with respect to modified suction, B_M is a scalar function for the

457 mechanical response and B_R is a scalar function for the retention response.

458 *3.1.1. Elastic behaviour*

459 Elastic behaviour under saturated or unsaturated conditions (STRPTH=1) is a particular

460 case of the general problem defined by Equations 35-38, noting that for STRPTH=1,

461 the mechanical and retention plastic multipliers are both zero.

462 Elastic behaviour is represented in the GCM in terms of the secant bulk $\bar{K}$ and shear $\bar{G}$

463 moduli, equivalent to saturated soils (Sheng et al., 2000). This representation ensures

464 the correct computation of Bishop's stresses at the intersection of the stress path with

465 one of the three yield curves of the model, when the computed response passes from

466 elastic to plastic. Integrating Equation 4 for p^* and ε_v^e the following analytical

467 expression for $\bar{K}$ can be found (Lloret-Cabot et al., 2016):

$$468 \quad \bar{K} = \frac{{}^i p^*}{\Delta\varepsilon_v^e}\left[\exp\left(\frac{{}^i v\left(1-\exp\left(-\Delta\varepsilon_v^e\right)\right)}{\kappa} \right) - 1 \right] \tag{39}$$

469 where ${}^i p^*$ and ${}^i v$ are, respectively, the mean Bishop's stress and specific volume at the

470 start of the volumetric strain increment i. A corresponding appropriate expression for

471 $\bar{G}$ should also be used (the form of this will depend upon what assumption is made for

472 the tangent shear modulus G, see Potts and Zdravkovic, 1999).

473 *3.1.2. Elasto-plastic behaviour*

474 Equations 35-38 are valid for all types of elasto-plastic yielding, including unsaturated

475 and saturated conditions, noting that, under saturated conditions, increases of S_r are

476 prevented.

477 Some useful simplifications are possible for the particular cases of yielding on one

478 water retention curve alone (STRPTH=2 or 3). Due to the absence of mechanical

479 yielding, p_0' remains unchanged which means that the mechanical plastic multiplier is

480 zero and then the increment of Bishop's stress can be computed exactly, using the

481 approach discussed for the elastic case. Also, given that $\Delta\lambda_M = 0$, it is possible to

482 compute exact values of degree of saturation at the updated exact value of modified

483 suction (Equation 33) using Equation 25 for yielding on only f_{WR} or Equation 26 for

484 yielding on only f_{DR}.

485 For mechanical yielding alone (STRPTH=4), whether the soil is saturated or

486 unsaturated, $\Delta\lambda_R = 0$ because $\Delta S_r = 0$. This means that the expression for $\Delta\lambda_M$ can be

487 found in the same way as that of the plastic multiplier for the MCC (see Sloan et al.,

488 (2001) for details).

489 Hence, the only two mechanisms that require the derivation of a new expression for the

490 mechanical and water retention plastic multipliers correspond to simultaneous yielding

491 on f_M and f_R (STRPTH=5 or 6). When f_M and f_R yield simultaneously, it is necessary to

492 impose the consistency condition on both to find expressions for $\Delta\lambda_M$ and $\Delta\lambda_R$ in terms

493 of $\Delta\boldsymbol{\varepsilon}$ and Δs:

494 $$df_M = 0 \;\Rightarrow\; \left(\frac{\partial f_M}{\partial \boldsymbol{\sigma}^*}\right)^T \mathbf{D_e}\left(\Delta\boldsymbol{\varepsilon}-\Delta\boldsymbol{\varepsilon}^\mathbf{p}\right)+\frac{\partial f_M}{\partial p_0^*}\left[\frac{\partial p_0^*}{\partial p'_0}\Delta p'_0+\frac{\partial p_0^*}{\partial S_r}\Delta S_r\right]=0 \qquad (40)$$

495 $$df_R = 0 \;\Rightarrow\; \left(\frac{\partial f_R}{\partial s^*}\right)\Delta s^*+\frac{\partial f_R}{\partial s_R^*}\left[\frac{\partial s_R^*}{\partial s_{R0}^*}\Delta s_{R0}^*+\frac{\partial s_R^*}{\partial p'_0}\Delta p'_0\right]=0 \qquad (41)$$

496 General expressions for the mechanical and retention plastic multipliers can be found

497 by solving simultaneously the above expressions, after inserting the relevant hardening

498 laws (Equations 9 and 21) and the relevant flow rules (Equations 10 and 24):

499 $$\Delta\lambda_M = \frac{\mathbf{D_M}\Delta\boldsymbol{\varepsilon}+C_M\Delta s^*}{A+\mathbf{D_M}\mathbf{a_M}} \qquad (42)$$

500 $$\Delta\lambda_R = \frac{D_R\Delta s^*+\mathbf{C_R}\Delta\boldsymbol{\varepsilon}}{A+\mathbf{D_M}\mathbf{a_M}} \qquad (43)$$

501 where $\mathbf{D_M}$, D_R, C_M, $\mathbf{C_R}$ and A are given by:

502 $$\mathbf{D_M} = \mathbf{a}_\mathbf{M}^T\mathbf{D_e} \qquad (44)$$

503 $$D_{\mathrm{R}} = \frac{-1}{B_{\mathrm{R}}} \left(\mathbf{D_M a_M} - \frac{\partial f_{\mathrm{M}}}{\partial p_0^*} \frac{\partial p_0^*}{\partial p'_0} B_{\mathrm{M}} \right) \frac{\partial s_{\mathrm{R0}}^*}{\partial s_{\mathrm{R}}^*} \qquad (45)$$

504 $$C_{\mathrm{M}} = \frac{1}{B_{\mathrm{R}}} \frac{\partial f_{\mathrm{M}}}{\partial p_0^*} \frac{\partial p_0^*}{\partial S_r} \frac{\partial s_{\mathrm{R0}}^*}{\partial s_{\mathrm{R}}^*} \frac{\partial f_{\mathrm{R}}}{\partial s^*} \qquad (46)$$

505 $$\mathbf{C_R} = \frac{B_{\mathrm{M}}}{B_{\mathrm{R}}} \left[\frac{\partial s_{\mathrm{R0}}^*}{\partial s_{\mathrm{R}}^*} \frac{\partial s_{\mathrm{R}}^*}{\partial p_0'} \right] \mathbf{D_M} \qquad (47)$$

506 $$A = -\left(1 - k_1 k_2\right) \frac{\partial f_{\mathrm{M}}}{\partial p_0^*} \frac{\partial p_0^*}{\partial p_0'} B_{\mathrm{M}} \qquad (48)$$

507 The expressions for the scalar functions B_{M} and B_{R} are:

508 $$B_{\mathrm{M}} = \frac{\partial p_0'}{\partial \varepsilon_v^p} \frac{\partial f_{\mathrm{M}}}{\partial p^*} \qquad (49)$$

509 $$B_{\mathrm{R}} = \frac{\partial s_{\mathrm{R0}}^*}{\partial S_r^p} \frac{\partial f_{\mathrm{R}}}{\partial s^*} \qquad (50)$$

510 As noted earlier, Δs^* can be computed exactly when $\Delta \varepsilon$ and Δs are known (Equation
511 34).

512 3.2. Algorithm for the identification of the model response

513 The reformulation of GCM has facilitated the development of an algorithm that
514 identifies, unambiguously, which is the model response activated by the given
515 increments $\Delta \varepsilon$ and Δs. Once the model response is known, all variables are updated
516 using the appropriate set of incremental relations derived in the previous section. In
517 such update, the algorithm automatically checks if the stress path intersects a yield
518 curve and, if so, finds the corresponding intersection by using the Pegasus algorithm
519 proposed by Dowell and Jarratt (1972), and widely tested for saturated soil models
520 (Sloan et al., 2001, Abbo, 1997, Sheng et al., 2000, Pedroso et al., 2008, Zhao et al.,
521 2005).

522 Figure 6 illustrates the various steps carried out by the algorithm to decide how to
523 integrate the given increments of $\Delta \varepsilon$ and Δs correctly. The case illustrated corresponds
524 to the most challenging scenario in which, from an initial point inside the elastic
525 domain, the known increments $\Delta \varepsilon$ and Δs end up activating yielding on two yield
526 curves. The particular model response plotted corresponds to STRPTH=6, but
527 equivalent results are obtained for STRPTH=5. A maximum of three different trials is

528   needed to handle correctly this problem. This means that, in the worst situation, the

529   algorithm needs to break $\Delta\boldsymbol{\varepsilon}$ and Δs in three parts. All other cases (i.e. initial stress point

530   on one or two yield curves) are a simplified version of this one and, hence, follow the

531   same logic.

532   Figure 6 is in two parts. Part a shows the full sequence of steps in the $\ln p_0':\ln s^*$ plane

533   whereas Part b illustrates their counterparts in the $S_r:\ln p^*$ plane (note that the values of

534   S_r in the vertical axis increase downwards). The current stress point is indicated by i

535   and is assumed to be inside the three yield curves of the model (note that ${}^i f_{\mathrm{WR}}$ is not

536   included in Figure 6a for clarity, but its location is to the left of point i, see Figure 5 for

537   reference). *Trial 1* (indicated by t_1) is purely elastic ($\Delta S_r = 0$ and $\Delta p_0' = 0$) and ends up

538   outside both ${}^i f_{\mathrm{DR}}$ (see Figure 6a) and ${}^i f_{\mathrm{M}}$ (see Figure 6b). Hence, it is necessary to check

539   which of these two yield curves is hit first by *trial 1*. This problem involves finding two

540   scalars (α_1 for f_{DR} and α_2 for f_{M}), both between 0 and 1, that indicate the portion of $\Delta\boldsymbol{\varepsilon}$

541   and Δs required to move, elastically, the stress point i to the corresponding intersection

542   point (indicated as i_{R1} for f_{DR} and i_{M1} for f_{M}). The lower value of the two scalars

543   corresponds to the yield curve hit first by *trial 1*. In the example represented in Figure

544   6, f_{DR} is the yield curve hit first (i.e. $\alpha_1 < \alpha_2$). Hence, a purely elastic update of the stress

545   point from i to the intersection point i_{R1} is then carried out using the appropriate portion

546   of the given increments (i.e. $\alpha_1\Delta\boldsymbol{\varepsilon}$ and $\alpha_1\Delta s$). The next step is to compute *Trial 2*

547   (indicated as t_2) starting from i_{R1} (also indicated as i_{R} in Figure 6) and now assuming

548   yielding on only f_{DR}. Importantly, *Trial 2* uses only the not yet integrated part of the

549   increments of strains and suction i.e. $(1-\alpha_1)\Delta\boldsymbol{\varepsilon}$ and $(1-\alpha_1)\Delta s$. Given that yielding on only

550   f_{DR} is the model response assumed in computing t_2, the mechanical hardening parameter

551   p_0' is constant (see Figure 6a) and the corresponding value of S_r is exact because it can

552   be calculated inserting the exact value of modified suction at t_2 (which equals that

553   calculated in t_1, see Figure 6a) in the equation of the main drying curve (Equation 26).

554   A second intersection problem arises, now with ${}^i f_{\mathrm{M}}$ (Figure 6). This second intersection

555   problem involves finding a scalar β (also between 0 and 1) that defines the portion of

556    $(1-\alpha_1)\Delta\boldsymbol{\varepsilon}$ and $(1-\alpha_1)\Delta s$ required to move, under yielding on only f_{DR}, the stress point

557   from i_{R} to i_{M} (also indicated as i_{Y} in Figure 6 to highlight that the stress point lies on

558   both yield curves). Once β has been found, the stress point is updated from i_{R} to i_{M}

559   assuming yielding on only f_{DR} and using the relevant portion of strain and suction

560   increments i.e. $\beta(1-\alpha_1)\Delta\boldsymbol{\varepsilon}$ and $\beta(1-\alpha_1)\Delta s$. In moving the stress point from i_{R} to i_{M},

561   yielding on only f_{DR} is occurring and, consequently, ${}^i f_{\mathrm{DR}}$ yields to ${}^Y f_{\mathrm{DR}}$ as indicated by

562 the thicker light dashed line in Figure 6a. At this stage, the stress point is on both yield

563 curves. A final *trial 3*, now assuming yielding on only f_M, needs to be computed to

564 determine whether the portion not yet integrated of strains and suction increments (i.e.

565 $(1-\beta)(1-\alpha_1)\Delta\varepsilon$ and $(1-\beta)(1-\alpha_1)\Delta s$) activates yielding on only f_M or simultaneous yielding

566 on f_M and f_{DR}. Conveniently, the algorithm *knows* at this point that yielding on only f_{DR}

567 is not possible because *trial 2* fell outside f_M when assuming yielding on only f_{DR}. In

568 the example of Figure 6, *trial 3* ends up outside $^Y f_{DR}$ meaning that this final portion of

569 $\Delta\varepsilon$ and Δs, moving the stress point from i_Y to $i+1$, has to be integrated assuming

570 simultaneous yielding on f_M and f_{DR}. The stress path followed to integrate the full size

571 of $\Delta\varepsilon$ and Δs is indicated in the figure by a thick black solid line and the final positions

572 of f_M and f_{DR} at $i+1$ are indicated by a lighter thick solid line.

573
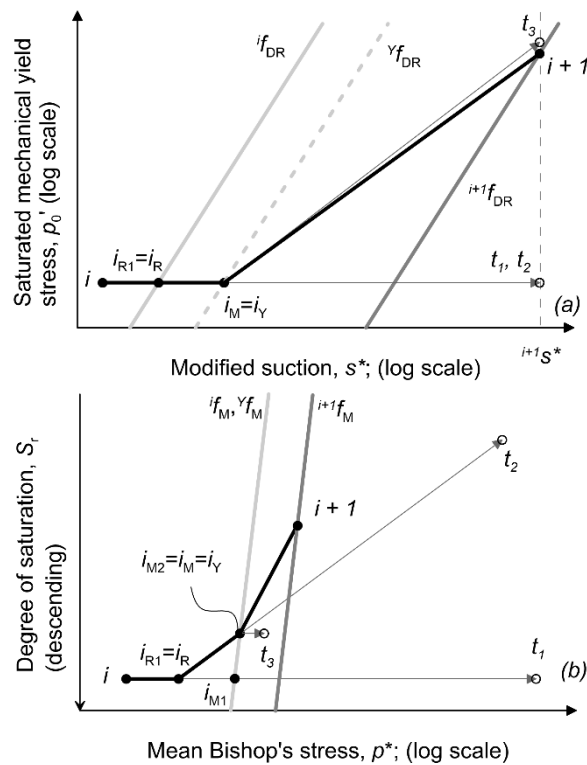
575 Figure 6 Example of a typical integration of the GCM starting from inside the three

576 yield curves and ending up activating yielding on two yield surfaces (STRPTH=6).

577

578 A more formalised description of the sequence of steps followed by the algorithm to

579 determine which is the active response of the GCM is presented in Appendix B.

580 3.3. Yield intersections

581   The given increments of $\Delta\boldsymbol{\varepsilon}$ and Δs may change the stress state from elastic to elasto-

582   plastic within the increment. In the context of the GCM, this means that a *trial* intersects

583   at least one yield curve. Note that during a transition from unsaturated to saturated

584   conditions, there might also be the reverse situation (i.e. from elasto-plastic to elastic

585   within an individual increment) in wetting paths that saturate during collapse

586   compression (Lloret-Cabot et al., 2017, Lloret-Cabot et al., 2018) i.e. it is possible to

587   have within a single increment a first part (while unsaturated) that is elasto-plastic and

588   a second part (while saturated) that is elastic. The intersection point in such cases is

589   controlled by the value of S_r but it is found in an equivalent way to any other intersection

590   problem. All of these intersections are found here using the Pegasus algorithm proposed

591   by Dowell and Jarratt (1972) and extensively used in the literature (e.g. Sloan et al.,

592   2001, Abbo, 1997, Sheng et al., 2000, Pedroso et al., 2008, Zhao et al., 2005). Its

593   algorithmic form is summarised in Appendix C for completeness).

594   There might situations in which the given increments of strain and suction intersect a

595   yield surface twice, even though initial and final stress states are both inside the yield

596   locus. Such situation is aggravated when using too large increments and, hence, the use

597   of sufficiently small increments of strain and suction is recommended. Sołowski &

598   Sloan (2012) discuss this intersection problem further in the context of the BBM

599   (Alonso et al. 1990).

600   Another possible intersection problem is that referred to as "elasto-plastic unloading"

601   (Sloan et al. 2001). The solution to this problem in the context of the GCM is equivalent

602   to that proposed for critical state saturated models (e.g. Sloan et al., 2001, Abbo, 1997,

603   Sheng et al., 2000, Pedroso et al., 2008).

604   3.4. Drift correction

605   Similarly to what is observed in explicit integration schemes for saturated soils, in

606   unsaturated soils too the stress point at the end of each integration step/substep may

607   *drift* from the yield condition, so that $|f_A| > FTOL$. The extent of this drift primarily

608   depends on the accuracy of the integration scheme used and, in general, when using

609   substepping strategies with error control, drift correction is rarely needed Sołowski et

610   al. (2012). However, as advised in Sloan et al. (2001), it is prudent to consider the

611   possibility to correct a potential drift at the end of each integrated step/substep.

612 In the context of the GCM, a correction of the drift of the stress point is only potentially

613 needed when mechanical yielding occurs, whether this implies yielding on only f_M

614 (STRPTH=4) or simultaneous yielding on f_M and a retention yield curve (STRPTH=5

615 or 6). Yielding on a retention yield curve alone (STRPTH=2 or 3) does not require any

616 drift correction in the context of strain-driven formulations because, as explained

617 earlier, an exact update of all relevant variables is possible.

618 The strategy to correct the stress point in the GCM adopts the drift correction method

619 recommended in Potts and Gens (1984) for saturated soils. The extension of such

620 strategy to unsaturated soils includes the assumption that, in addition to imposing no

621 strain variations i.e. $\delta\boldsymbol{\varepsilon} = \mathbf{0}$ during the correction of the stress point, also suction remains

622 unchanged i.e. $\delta s = 0$. The latter assumption has been successfully used for the

623 numerical integration of many other unsaturated soil models (e.g. Sánchez et al. 2008,

624 Sołowski and Gallipoli 2010ab).

625 Assuming $\delta\boldsymbol{\varepsilon} = \mathbf{0}$ and $\delta s = 0$ means that the correction of modified suction δs^* and

626 specific volume δv are both zero. Given that $\delta s^* = 0$, the correction of degree of

627 saturation δS_r and of the water retention hardening parameters $\delta s_{R0}{}^*$ are all also zero.

628 The correction of Bishop's stresses $\delta\boldsymbol{\sigma}^*$ and mechanical hardening parameter $\delta p_0'$ are

629 unknown quantities and can be found by expanding f_M in Taylor series about the stress

630 point to be corrected i. Neglecting second order terms and above, this can be expressed

631 by:

632
$$f_\text{M} \approx {}^i f_\text{M} + {}^i\left(\frac{\partial f_\text{M}}{\partial \boldsymbol{\sigma}^*}\right)\delta\boldsymbol{\sigma}^* + {}^i\left(\frac{\partial f_\text{M}}{\partial p_0^*}\right)\left(\frac{\partial p_0^*}{\partial p_0'}\delta p_0' + \frac{\partial p_0^*}{\partial S_r}\delta S_r\right) \tag{51}$$

633 where $\delta S_r = 0$.

634 Equations 35 and 36 mean that for the total strain increment to remain zero, the

635 corrections in the Bishop's stress and mechanical hardening parameter are,

636 respectively:

637
$$\delta\boldsymbol{\sigma}^* = -\delta\lambda_\text{M}\mathbf{D_e}\mathbf{a_M} \tag{52}$$

638
$$\delta p_0' = \delta\lambda_\text{M}B_\text{M} \tag{53}$$

639 where $\delta\lambda_\text{M}$ is an unknown multiplier and $\mathbf{D_e}$, $\mathbf{a_M}$ and B_M are all evaluated at i.

640 The following expression for $\delta\lambda_\text{M}$ is found by combining Equations 51-53, after

641 imposing that $f_\text{M} = 0$:

642 $$\delta\lambda_M = \frac{f_M}{\mathbf{a}^T\mathbf{D_e}\mathbf{a} - \frac{\partial f_M}{\partial p_0^*}\frac{\partial p_0^*}{\partial p_0{}'}B_M} \qquad (54)$$

643 While there is no need to correct s^*, $s_{R0}{}^*$, S_r nor v, a correction needs to be applied to

644 the mechanical and the water retention yield stresses:

645 $$\delta p_0^* = \frac{p_0^*}{p_0{}'}\delta\lambda_M B_M \qquad (55)$$

646 $$\delta s_R^* = k_2\frac{s_R^*}{p_0{}'}\delta\lambda_M B_M \qquad (56)$$

647 where all variables are evaluated at i.

648   4. EXPLICIT SUBSTEPPING INTEGRATION SCHEMES

649 This section presents two explicit substepping integration schemes for the numerical

650 integration of the GCM. The first one corresponds to the second order accurate

651 modified Euler with substepping (ME2) whereas the second one is the fifth order

652 accurate Runge-Kutta-Dormand-Prince (RKDP5) with substepping. The notation

653 adopted extends that employed by Sloan et al. (2001) to unsaturated soils, making

654 explicit the dependence of the initial value problem (IVP) on the specific volume (as in

655 critical state models for saturated soils, see Lloret-Cabot et al., 2016) and also on the

656 degree of saturation. A comparative analysis of the relative numerical performance of

657 these two substepping integration schemes is provided in the next section.

658 For the same reasons given in the drift correction approach, the application of a

659 substepping strategy with error control in the GCM is unnecessary in absence of

660 mechanical yielding, whether this means elastic behaviour or yielding on only one

661 retention curve (i.e. STRPTH=1, 2 or 3). In contrast, a substepping strategy with error

662 control becomes extremely convenient for the numerical integration of the incremental

663 relations of the GCM when mechanical yielding is active, because for STRPTH=4, 5

664 or 6 the incremental constitutive laws are not integrable analytically. In such cases, the

665 key to ensure an accurate and efficient numerical integration is to control the local error

666 in the computed variables arising due to the inexact integration of the integration

667 scheme. In a substepping integration scheme, this local error is controlled by using a

668 measure of the truncation error, which is estimated as the difference between the

669 approximate solutions from two integration schemes of different order (Shampine,

670   1994). How much these two approximations differ from each other is indicative of the

671   deviation of the numerical solution from the true solution and, hence, this difference

672   can be used to estimate the truncation error and to automatically adjust, then, the size

673   of the current integration step/substep.

674   To extend to unsaturated conditions the formulation of Sloan et al. (2001) presented for

675   saturated soils, it is useful to express the equations involved in the problem in terms of

676   a pseudo-time T:

677
$$T = \frac{t - {}^{i=0}t}{\Delta t} \tag{57}$$

678   where $t = {}^{i=0}t$ is the time at the start of the strain increment $\Delta\boldsymbol{\varepsilon}$ and suction increment Δs

679   (i.e. $T = 0$), $t = {}^{0}t + \Delta t$ is the time at the end of the strain and suction increments (i.e. T

680     $= 1$) and $0 \leq T \leq 1$.

681
$$\frac{\mathrm{d}s}{\mathrm{d}T} \cong \Delta s \tag{58}$$

682
$$\frac{\mathrm{d}v}{\mathrm{d}T} \cong v \exp\left(-\Delta\varepsilon_{\mathrm{v}}\right) \tag{59}$$

683
$$\frac{\mathrm{d}s^{*}}{\mathrm{d}T} \cong \Delta s^{*} \tag{60}$$

684
$$\frac{\mathrm{d}\boldsymbol{\sigma}^{*}}{\mathrm{d}T} \cong \Delta\boldsymbol{\sigma}^{*} = \mathbf{D}_{\mathrm{e}}\Delta\boldsymbol{\varepsilon} - \Delta\lambda_{\mathrm{M}}\mathbf{D}_{\mathrm{e}}\mathbf{a}_{\mathrm{M}} \tag{61}$$

685
$$\frac{\mathrm{d}p_{0}{}'}{\mathrm{d}T} \cong \Delta p_{0}{}' = \Delta\lambda_{\mathrm{M}}B_{\mathrm{M}} \tag{62}$$

686
$$\frac{\mathrm{d}S_{r}}{\mathrm{d}T} \cong \Delta S_{r} = -\Delta\lambda_{\mathrm{R}}a_{\mathrm{R}} \tag{63}$$

687
$$\frac{\mathrm{d}s_{\mathrm{R0}}^{*}}{\mathrm{d}T} \cong \Delta s_{\mathrm{R0}}^{*} = \Delta\lambda_{\mathrm{R}}B_{\mathrm{R}} \tag{64}$$

688   where the subscript "$_{\mathrm{R}}$" is 1 for f_{WR} and 2 for f_{DR}.

689   The system of Equations 58-64 defines an initial value problem (IVP) that can be

690   integrated over T knowing the values at the initial (or current) state i of modified suction

691     ${}^{i}s^{*}$, Bishop's stress ${}^{i}\boldsymbol{\sigma}^{*}$, hardening parameters ${}^{i}p_{0}{}'$ and ${}^{i}s_{\mathrm{R0}}^{*}$, specific volume ${}^{i}v$ and degree

692   of saturation ${}^{i}S_{r}$, together with the imposed $\Delta\boldsymbol{\varepsilon}$ and Δs. Similarly to the strain-driven

693   numerical integration of the MCC for $\Delta\boldsymbol{\varepsilon}$, also Δs is fixed in the strain-driven integration

694   of the GCM presented here, meaning that the IVP is solved assuming constant strain

695   and suction rates, $\Delta\boldsymbol{\varepsilon}/\Delta t$ and $\Delta s/\Delta t$, during each step/substep.

696 The form of the system of equations 59-64 is a direct consequence of assuming that not
697 only the mechanical behaviour of unsaturated soils can be represented as an elasto-
698 plastic process but also the water retention response (Wheeler et al. 2003). Under these
699 considerations, the system of equations 59 to 64 encompasses saturated and unsaturated
700 conditions and incorporates the coupling between the mechanical and the water
701 retention behaviour. Although the specific GCM equations are used, the same
702 integration scheme is applicable to any model that, in addition to assuming elasto-
703 plastic formulations for the mechanical and the water retention responses, accounts for
704 the coupling between mechanical and water retention behaviour via plastic volumetric
705 strains and plastic changes of degree of saturation.

706 A substepping integration scheme integrates the incremental relations of a constitutive
707 model by automatically adjusting the size of the given integration interval (or
708 increment) depending on a relative measure of the local error, REL. When REL is
709 larger/smaller than a specified tolerance (i.e. $STOL$), the current size of the integration
710 step/substep is reduced/increased according to $^{i+1}(\Delta T)=r\ ^{i}(\Delta T)$ where the scalar r is
711 estimated as follows. Based on the assumption that the size of a step/substep varies
712 proportionally to a measure of the local error r, Sloan et al. (2001) suggest to use $r \cong$
713 $0.9(STOL/REL_n)^{1/2}$ for the second order accurate modified Euler with substepping and
714 $r \cong 0.9(STOL/REL_n)^{1/5}$ for the fifth order accurate Runge-Kutta-Dormand-Prince with
715 substepping. An additional constraint for the scalar r is to bound its values between 0.1
716 and 1.1 to limit the change in size during two consecutive substeps, and a maximum
717 number of substeps needs to be also specified (see Sloan et al. (2001) for full details).

718 A major point of the substepping integration schemes presented here is that the measure
719 of the relative error REL is estimated for $\boldsymbol{\sigma}^*$, p_0', S_r and s_{R0}^*. The reason for treating
720 these variables separately is because the estimated values of the respective local error
721 for mechanical ($\boldsymbol{\sigma}^*$ and p_0') and water retention responses (S_r and s_{R0}^*) can have different
722 magnitudes. Hence, it is important for an efficient integration of a problem involving
723 unsaturated soils that when substepping integration schemes with automatic error
724 control are used, the error measure REL is estimated accounting for all major sources
725 of error, and for unsaturated soils these should include the local error arising during the
726 numerical integration of both mechanical and water retention constitutive relations. In
727 the two substepping integration schemes presented here, this measure of relative local

728 error *REL* is estimated by taking the difference between the higher order accurate and
729 the lower order accurate approximations for $\boldsymbol{\sigma}^*$, p_0', S_r and $s_{R0}{}^*$. Each of these
730 differences is then divided by the corresponding higher order approximation (indicated
731 by a hat in Equation 65). For the modified Euler with substepping this corresponds to
732 the difference between second order accurate modified Euler and first order accurate
733 forward Euler. For the RKDP5 with substepping, *REL* is calculated from fourth and
734 fifth Runge-Kutta-Dormand-Prince approximations.

735 Equivalently to what is proposed in Sloan et al. (2001) for saturated soils, *REL* takes
736 the maximum of these four relative measures of the step/substep error as a way to bound
737 the local error:

738
$$
REL = max\left\{ \frac{\left[\left(\hat{\boldsymbol{\sigma}}^* - \boldsymbol{\sigma}^* \right)^T \left(\hat{\boldsymbol{\sigma}}^* - \boldsymbol{\sigma}^* \right) \right]^{1/2}}{\left[\left(\hat{\boldsymbol{\sigma}}^* \right)^T \left(\hat{\boldsymbol{\sigma}}^* \right) \right]^{1/2}}, \frac{\left| \hat{p}_0{}' - p_0{}' \right|}{\hat{p}_0{}'}, \frac{\left| \hat{S}_r - S_r \right|}{\hat{S}_r}, \frac{\left| \hat{s}_{R0}^* - s_{R0}^* \right|}{\hat{s}_{R0}^*} \right\}
\tag{65}
$$

4.1. Modified Euler with substepping

740 Given a pseudo-time step/substep $^i(\Delta T)$ with $0 < {}^i(\Delta T) \leq 1$, the forward Euler and
741 modified Euler updates for $\boldsymbol{\sigma}^*$, p_0', S_r and $s_{R0}{}^*$ are described in the following by adopting
742 the Butcher tableau (Dormand and Prince, 1980). The coefficients for the two methods
743 are summarised in Table 1. The subscripts i and $i+1$ denote quantities evaluated at
744 pseudo-times ^iT and $^{i+1}T = {}^iT + {}^i(\Delta T)$ respectively:

745
$$
{}^{i+1}s = {}^is + {}^i\Delta s
\tag{66}
$$

746
$$
{}^{i+1}v = {}^iv \exp\left(-{}^i\Delta\varepsilon_v \right)
\tag{67}
$$

747
$$
{}^{i+1}s^* = {}^{i+1}s \frac{{}^{i+1}v - 1}{{}^{i+1}v}
\tag{68}
$$

748
$$
{}^{i+1}\boldsymbol{\sigma}^* = {}^i\boldsymbol{\sigma}^* + \sum_{k=1}^{n_s} {}^kb^k \Delta\boldsymbol{\sigma}^*
\tag{69}
$$

749 $$^{i+1}p_0{}' = {}^{i}p_0{}' + \sum_{k=1}^{n_s} {}^{k}b\, {}^{k}\Delta p_0{}'$$ (70)

750 $$^{i+1}S_r = {}^{i}S_r + \sum_{k=1}^{n_s} {}^{k}b\, {}^{k}\Delta S_r$$ (71)

751 $$^{i+1}s_{R0}^* = {}^{i}s_{R0}^* + \sum_{k=1}^{n_s} {}^{k}b\, {}^{k}\Delta s_{R0}^*$$ (72)

752 where the coefficients ^{k}b are summarised in Table 1, n_s is the number of stages of the

753 integration scheme, and

754
$$\left.\begin{aligned}
{}^{k}\Delta s^* &= {}^{i+1}s^* - {}^{i}s^* \\
{}^{k}\Delta\boldsymbol{\sigma}^* &= {}^{k}\mathbf{D}_e\, {}^{i}\Delta\boldsymbol{\varepsilon} - {}^{k}\Delta\lambda_M\, {}^{k}\mathbf{D}_e\, {}^{k}\mathbf{a}_M \\
{}^{k}\Delta p_0{}' &= {}^{k}\Delta\lambda_M\, {}^{k}B_M \\
{}^{k}\Delta S_r &= -{}^{k}\Delta\lambda_R\, a_R \\
{}^{k}\Delta s_{R0}^* &= {}^{k}\Delta\lambda_R\, {}^{k}B_R \\
{}^{i}\Delta s &= {}^{i}(\Delta T)\Delta s \\
{}^{i}\Delta\boldsymbol{\varepsilon} &= {}^{i}(\Delta T)\Delta\boldsymbol{\varepsilon}
\end{aligned}\right\} \quad \text{for } k = 1,\ldots n_s$$ (73)

755 where $\mathbf{D}_e$, $\mathbf{a}_M$, $\Delta\lambda_M$, $\Delta\lambda_R$, B_M and B_R are evaluated at k using:

756
$$\left.\begin{aligned}
{}^{k}\hat{s} &= {}^{i}s + \sum_{j=1}^{k-1} {}^{kj}a\, {}^{i}(\Delta T)\Delta s \\
{}^{k}\hat{v} &= {}^{i}v \exp\left(-\sum_{j=1}^{k-1} {}^{kj}a\, {}^{i}(\Delta T)\Delta\varepsilon_v\right) \\
{}^{k}\hat{s}^* &= {}^{k}\hat{s}\,\frac{{}^{k}\hat{v}-1}{{}^{k}\hat{v}} \\
{}^{k}\hat{\boldsymbol{\sigma}}^* &= {}^{i}\boldsymbol{\sigma}^* + \sum_{j=1}^{k-1} {}^{kj}a\, {}^{j}\Delta\boldsymbol{\sigma}^* \\
{}^{k}\hat{p}_0{}' &= {}^{i}p_0{}' + \sum_{j=1}^{k-1} {}^{kj}a\, {}^{j}\Delta p_0{}' \\
{}^{k}\hat{S}_r &= {}^{i}S_r + \sum_{j=1}^{k-1} {}^{kj}a\, {}^{j}\Delta S_r \\
{}^{k}\hat{s}_{R0}^* &= {}^{i}s_{R0}^* + \sum_{j=1}^{k-1} {}^{kj}a\, {}^{j}\Delta s_{R0}^*
\end{aligned}\right\} \quad \text{for } k = 1,\ldots,n_s$$ (74)

757 and the coefficients ^{kj}a are summarised in Table 1.

758 Lloret-Cabot et al. (2016) demonstrate, for critical state models for saturated soils, the
759 importance of ensuring that the update of v is consistent (i.e. at the same integration
760 portion of $\Delta\varepsilon$) with the update of effective stresses $\boldsymbol{\sigma}'$ and hardening parameter p_0'. An
761 equivalent logic applies to integration of critical state models for unsaturated soils that
762 account for mechanical and water retention behaviour where not only v, but also S_r
763 needs to be updated rigorously (i.e. now at the same integration portion of both $\Delta\varepsilon$ and
764 Δs) with the update of $\boldsymbol{\sigma}^*$, s^*, p_0' and $s_{R0}{}^*$ (Equation 74).

765 Strain-driven formulations allow for the exact computation of specific volume, matric
766 suction and modified suction at the end of the step/substep because it is possible to
767 integrate them analytically over $^i\Delta T$ to find the precise values of v, s and s^* at $i+1$. The
768 corresponding second order accurate updates for $\boldsymbol{\sigma}^*$, p_0', S_r and $s_{R0}{}^*$ are respectively
769 given by Equations 69-72 where $^1\Delta\boldsymbol{\sigma}^*$, $^1\Delta p_0'$, $^1\Delta S_r$ and $^1\Delta s_{R0}^*$ correspond to the
770 forward Euler increments and, $^2\Delta\boldsymbol{\sigma}^*$, $^2\Delta p_0'$, $^2\Delta S_r$ and $^2\Delta s_{R0}^*$ are computed using first
771 order updated variables (see Equations 73 and 74). If the step/substep is accepted, the
772 variables $\boldsymbol{\sigma}^*$, p_0', S_r and $s_{R0}{}^*$ are updated using the higher order approximation (i.e. *local*
773 *extrapolation* see Shampine, 1994).

774 Table 1. Coefficients for the forward Euler and modified Euler integration schemes
775 (Dormand and Prince, 1980)

^kc	^{kj}a					$^k\hat{b}$ (2nd)	^kb (1st)
0						1/2	1
1	1					1/2	0

776 4.2. Runge-Kutta-Dormand-Prince (RKDP) with substepping

777 The explicit Runge-Kutta-Dormand-Prince (RKDP) with substepping is applied here to
778 integrate the mechanical and water retention relations of the GCM for STRPTH= 4, 5
779 and 6. When applying this scheme to Equations 58-64, the same Equations 66-74 are
780 obtained but, for this method, the coefficients ^kb and ^{kj}a correspond to those summarised
781 in Table 2.

782 The RKDP scheme with substepping gives very accurate values for $^{i+1}\boldsymbol{\sigma}^*$, $^{i+1}p_0'$, $^{i+1}S_r$

783 and $^{i+1}s_{R0}{}^*$ at the end of each step/substep, at the expense of additional evaluations of

784 the constitutive relations. In the absence of an analytical solution, these highly accurate

785 approximations are used as a *reference* to check the accuracy of lower order methods.

786 Table 2. Coefficients for the RKDP4 and RKDP5 integration schemes (Dormand and

787 Prince, 1980)

$^k c$	$^{kj} a$					$^k \hat{b}$ (5th)	$^k b$ (4th)
0						19/216	31/540
1/5	1/5					0	0
3/10	3/40	9/40				1000/2079	190/297
3/5	3/10	-9/10	6/5			-125/216	-145/108
2/3	226/729	-25/27	880/729	55/729		81/88	351/220
1	-181/270	5/2	-266/297	-91/27	189/55	5/56	1/20

788 5. VERIFICATION AND COMPUTATIONAL ASPECTS

789 The variation of the local error with the size of the integrated increments depends on

790 the order of local accuracy of the numerical method used. Based on this information,

791 Lloret-Cabot et al. (2016) propose a verification method for the numerical integration

792 of constitutive models for saturated soils. This verification strategy is especially

793 convenient for explicit substepping integration schemes, because it first checks the

794 expected behaviour of the error at the level of one single step/substep and it then checks

795 the theoretical response of the cumulative error over several substeps.

796 As demonstrated here, the same strategy can be adapted to study the behaviour of the

797 error in the numerical integration of models for unsaturated soils. In the development

798 presented hereafter, e refers to the error incurred by the numerical scheme in a single

799 substep (or step in the case of no substepping) and E is the cumulative error over a

800 number of substeps. Note that the error control in a substepping strategy only controls

801 the error in a single substep, with the aim of controlling the cumulative error over

802 several steps.

803 To study the behaviour of the local error when numerically integrating a model, it is

804 useful to compare the approximations given by the integration scheme against a

805 reference or, when possible, an analytical solution. Given that the GCM involves

806 mechanical and water retention behaviour, it is necessary to study the magnitude of the

807 error not only in the mechanical response (as shown in Lloret-Cabot et al. (2016) for

808 the saturated MCC) but also in the water retention response. Consequently, the

809 assessment of the error investigated here for the integration of the GCM will include

810 the relative error incurred in the approximated mechanical response (in terms of

811 Bishop's stresses $\boldsymbol{\sigma}^*$ and mechanical hardening parameter p_0') and the approximated

812 water retention response (in terms of degree of saturation S_r and a water retention

813 hardening parameter s_{R0}^*) when varying the size of $\Delta\boldsymbol{\varepsilon}$, Δs or both. The relative error in

814 each of these variables in a single substep/step is computed as:

815
$$e_{\boldsymbol{\sigma}^*} = \frac{\left\{\left(\boldsymbol{\sigma}_{ref}^* - \boldsymbol{\sigma}^*\right)^T \left(\boldsymbol{\sigma}_{ref}^* - \boldsymbol{\sigma}^*\right)\right\}^{1/2}}{\left\{\left(\boldsymbol{\sigma}_{ref}^*\right)^T \left(\boldsymbol{\sigma}_{ref}^*\right)\right\}^{1/2}} \tag{75}$$

816
$$e_{S_r} = \frac{\left| S_{rref} - S_r \right|}{S_{rref}} \tag{76}$$

817
$$e_{p_0'} = \frac{\left| p_{0ref}' - p_0' \right|}{p_{0ref}'} \tag{77}$$

818
$$e_{s_{R0}^*} = \frac{\left| s_{R0ref}^* - s_{R0}^* \right|}{s_{R0ref}^*} \tag{78}$$

819 where the subscript *ref* indicates a reference solution (or, when available, analytical).

820 5.1. Relative error in a single-step

821 Two numerical tests are carried out to study how the error in $\boldsymbol{\sigma}^*$, S_r, p_0' and s_{R0}^*

822 propagates during a single integration step (i.e. with no substepping) using the second

823 order modified Euler (ME2) and the fifth order Runge-Kutta-Dormand-Prince

824 (RKDP5) integration schemes. Both tests assume axisymmetric conditions and consider

825 an initial unsaturated stress state lying on both mechanical and wetting retention yield

826 curves, at zero deviatoric stress. The soil constants and initial state considered in all the

827 simulations are summarised in Tables 3 and 4, respectively. This initial state gives

828   initial values of specific volume and degree of saturation $v = 2.20$, $S_r = 0.65$. Further

829   details on model parameters and initial state of GCM are found in Lloret-Cabot et al.

830   (2017). The tolerance associated with yield surface intersections and the correction of

831   the stresses back to the yield curve, *FTOL*, is assumed equal to 10^{-12}.

832   Table 3. Values of soil constants for the GCM simulations for Tests A, B and C

$\lambda = 0.15$	$\kappa = 0.02$	N = 2.73	$R = 1.4$	M = 1.20
$N^* = 2.90$	$k_1 = 0.70$	$k_2 = 0.80$	$\lambda_s = 0.12$	$\upsilon = 0.33$ [(*)]

833
834   [(*)] where υ is the Poisson's ratio (tangent and secant values of shear modulus were calculated from the corresponding tangent and secant values of bulk modulus by assuming a constant value of Poisson's ratio.

835   Table 4. Initial state for GCM simulations for Tests A and B (see the Appendix A)

$p^* = 200\,\text{kPa}$	$q = 0\,\text{kPa}$	$p_0^* = 200\,\text{kPa}$
$s^* = 109.09\,\text{kPa}$	--	$s_1^* = 109.09\,\text{kPa}$

836   The reason for considering this type of initial state (with $p^* = p^*_0$ and $s^* = s_1^*$) is because

837   when positive increments of strain (loading) and/or decrements of matric suction

838   (wetting) are applied from the assumed initial state, simultaneous yielding on the

839   mechanical and wetting retention yield curves (STRPTH=5) is activated which

840   corresponds to the desired situation in which the numerical approximation of all four

841   variables investigated contain some amount of error.

842   The first numerical test (Test A) studies the variation of the error for given finite equal

843   variations of axial strain and radial strain $\Delta\varepsilon_a = \Delta\varepsilon_r \approx \Delta\varepsilon_v/3$ (where $\Delta\varepsilon_v$ is the increment

844   of volumetric strain) with no variation of suction (i.e. isotropic straining at constant

845   suction). The second test (Test B) studies the error response for a combined axial strain

846   increment $\Delta\varepsilon_a$ (with no radial strains, $\Delta\varepsilon_r$) and a finite decrement of suction $-\Delta s$ (i.e.

847   axial straining under wetting).

848   Test A computes the error by comparing the numerical approximation against the

849   corresponding analytical solution. This comparison provides, hence, a clear and

850   unambiguous interpretation of the error results. Conversely, Test B compares the

851   numerical approximation against a reference solution (obtained by using the RKDP

852   scheme with substepping and very stringent tolerances). In the two numerical tests

853   presented, the size of the assumed input increments of strains and suction are varied to

854   study how such variation in size influences the error in the solution. For Test A, the

855   volumetric strain increment size analysed varies from $\Delta\varepsilon_v = 10^{-06}$ to 0.1 (with $\Delta s = 0$).

856   For Test B, the increment sizes varied from $\Delta\varepsilon_a = 10^{-06}$ and $\Delta s = -10^{-06}$ kPa to $\Delta\varepsilon_a =$

857   0.01 and $\Delta s = -0.01$kPa (keeping $\Delta\varepsilon_r = 0$).

858   Accuracy in each numerical method is assessed by plotting the error in $\boldsymbol{\sigma}^*$, S_r, p_0' and

859   s_{10}^* against the size of the input of strain or suction variations using logarithmic scales.

860   This form of plotting the error results provides a first form of verification of an

861   integration scheme, because the gradient obtained for the best-fitted straight line

862   through a particular set of error results (i.e. all belonging to approximations from the

863   same integration scheme) should be in correspondence with the order of accuracy of

864   the numerical integration method (Lloret-Cabot et al., 2016).

865   Figures 7 and 8 illustrate the behaviour of the relative error for Tests A and B

866   respectively, for a single step. Each figure is in four parts. The response of the relative

867   error for the mechanical behaviour is shown in Parts (a) and (c), in terms of Bishop's

868   stress $\boldsymbol{\sigma}^*$ and mechanical hardening parameter p_0', respectively. Parts (b) and (d) show

869   the response of the relative error for the water retention behaviour in terms of degree of

870   saturation S_r and wetting retention hardening parameter s_{10}^*, respectively. In the figures,

871   symbols indicate the computed relative error and the dashed lines indicate the best-

872   fitted straight line through the computed relative error for the same numerical method.

873   Typical error results for Test A when using the ME2 and RKDP5 schemes, respectively,

874   are summarised in Tables 5 and 6.

875   Table 5. Typical relative error values in Bishop's stress $\boldsymbol{\sigma}^*$, degree of saturation S_r,

876   mechanical hardening parameter p_0' and wetting retention hardening parameter s_{10}^* for

877   a single elasto-plastic isotropic loading step at constant suction for the modified Euler

878   with substepping (ME2) considering $STOL = 1$.

$\Delta\varepsilon_v$	Error in $\boldsymbol{\sigma}^*$	Error in S_r	Error in p_0'	Error in s_{10}^*
$1\cdot10^{-06}$	$< 1.0\cdot10^{-15}$	$< 1.0\cdot10^{-15}$	$< 1.0\cdot10^{-15}$	$< 1.0\cdot10^{-15}$
$1\cdot10^{-05}$	$4.50\cdot10^{-14}$	$< 1.0\cdot10^{-15}$	$6.74\cdot10^{-13}$	$5.41\cdot10^{-13}$
$1\cdot10^{-04}$	$4.37\cdot10^{-11}$	$2.15\cdot10^{-13}$	$6.72\cdot10^{-10}$	$5.38\cdot10^{-10}$
$1\cdot10^{-03}$	$4.35\cdot10^{-08}$	$2.14\cdot10^{-10}$	$6.64\cdot10^{-07}$	$5.31\cdot10^{-07}$
$1\cdot10^{-02}$	$4.10\cdot10^{-05}$	$2.09\cdot10^{-07}$	$5.89\cdot10^{-04}$	$4.72\cdot10^{-04}$
$1\cdot10^{-01}$	$1.39\cdot10^{-02}$	$9.00\cdot10^{-05}$	$1.30\cdot10^{-01}$	$1.18\cdot10^{-01}$

879   Table 6. Typical relative error values in Bishop's stress σ^*, degree of saturation S_r,

880   mechanical hardening parameter p_0' and wetting retention hardening parameter s_{10}^* for

881   a single elasto-plastic isotropic loading step at constant suction for Runge-Kutta-

882   Dormand-Prince with substepping (RKDP5) considering *STOL*=1.

$\Delta\varepsilon_v$	Error in σ^*	Error in S_r	Error in p_0'	Error in s_{10}^*
$1 \cdot 10^{-06}$	$< 1.0 \cdot 10^{-15}$	$< 1.0 \cdot 10^{-15}$	$< 1.0 \cdot 10^{-15}$	$< 1.0 \cdot 10^{-15}$
$1 \cdot 10^{-05}$	$< 1.0 \cdot 10^{-15}$	$< 1.0 \cdot 10^{-15}$	$< 1.0 \cdot 10^{-15}$	$< 1.0 \cdot 10^{-15}$
$1 \cdot 10^{-04}$	$< 1.0 \cdot 10^{-15}$	$< 1.0 \cdot 10^{-15}$	$< 1.0 \cdot 10^{-15}$	$< 1.0 \cdot 10^{-15}$
$1 \cdot 10^{-03}$	$< 1.0 \cdot 10^{-15}$	$< 1.0 \cdot 10^{-15}$	$< 1.0 \cdot 10^{-15}$	$< 1.0 \cdot 10^{-15}$
$1 \cdot 10^{-02}$	$1.02 \cdot 10^{-11}$	$< 1.0 \cdot 10^{-15}$	$2.39 \cdot 10^{-09}$	$1.91 \cdot 10^{-09}$
$1 \cdot 10^{-01}$	$6.94 \cdot 10^{-06}$	$5.31 \cdot 10^{-12}$	$1.33 \cdot 10^{-03}$	$1.06 \cdot 10^{-03}$

883   The respective gradients of each best-fitted straight line plotted in both figures match

884   the expected order of accuracy of the method, suggesting that both substepping schemes

885   work correctly at a single step/substep level. In particular, for both tests, approximate

886   gradients of 6 are obtained when best-fitting a straight line through the computed error

887   values in σ^*, S_r, p_0' and s_{10}^* corresponding to the RKDP5 method and approximate

888   gradients of 3 are obtained when best-fitting a straight line through the computed error

889   values in σ^*, S_r, p_0' and s_{10}^* corresponding to the ME2 method. Note that, for

890   completeness, Figures 7 and 8 also include the best-fitted lines for the computed error

891   values for the single-step first order forward Euler (gradient 2) and single-step fourth

892   order Runge-Kutta-Dormand-Prince (gradient 5) integration schemes, in addition to the

893   error results for ME2 and RKDP5.

894   The results in Figures 7 and 8 show that the specific values of the local relative error

895   incurred in each variable considered during the numerical integration, differ in each

896   numerical test considered. In particular, the variation of the position of each best-fitted

897   line (i.e. intercept) differs in each test and for each variable considered. This behaviour

898   justifies the decision of treating separately the local error from mechanical (i.e. σ^* and

899   p_0') and water retention (i.e. S_r and s_{10}^*) responses.
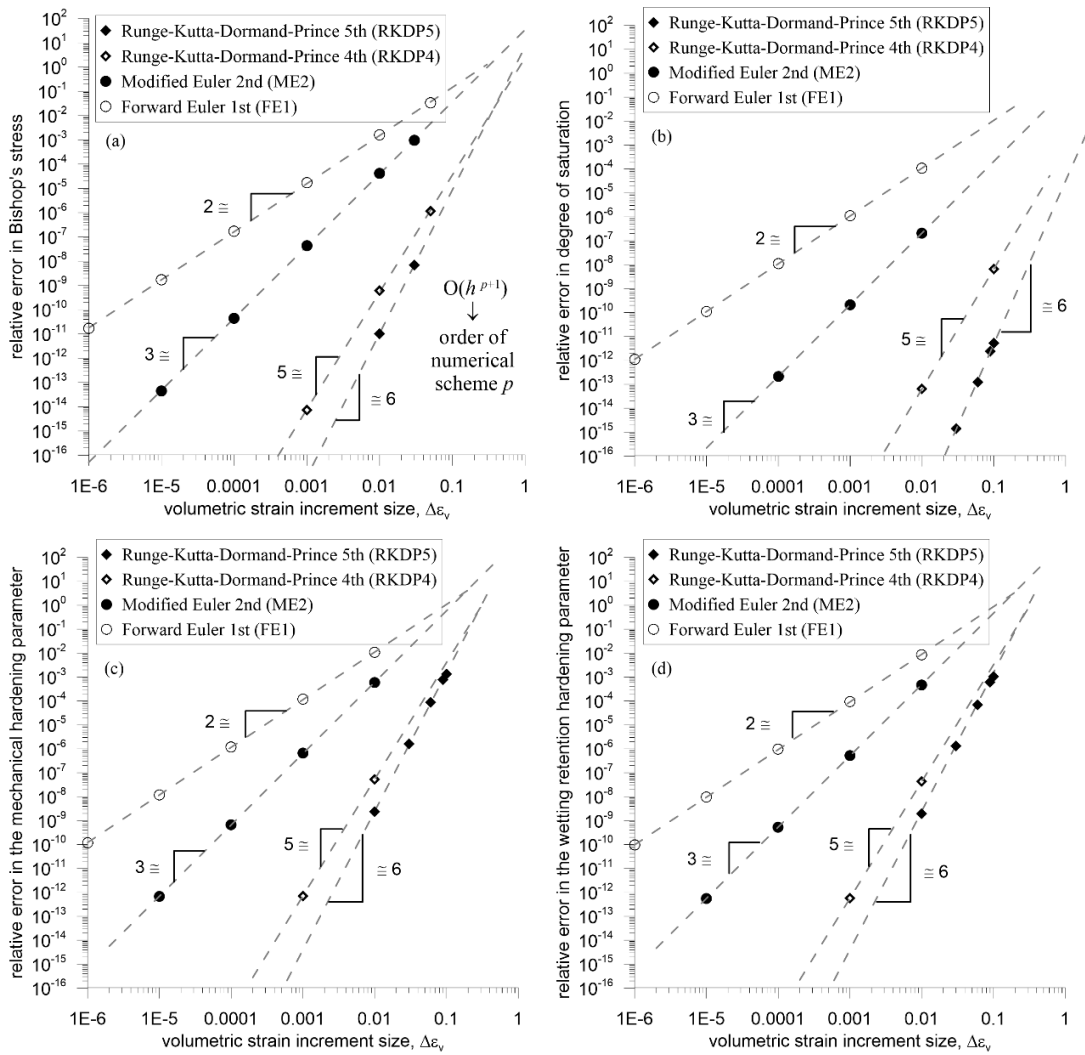
900 Figure 7. Relative error for single-step explicit integration schemes against volumetric
901 strain increment size for a single elasto-plastic isotropic strain increment at constant
902 suction: (a) Bishop's stress σ^*; (b) degree of saturation S_r; (c) mechanical hardening
903 parameter p_0'; (d) water retention hardening parameter s_{10}^*.
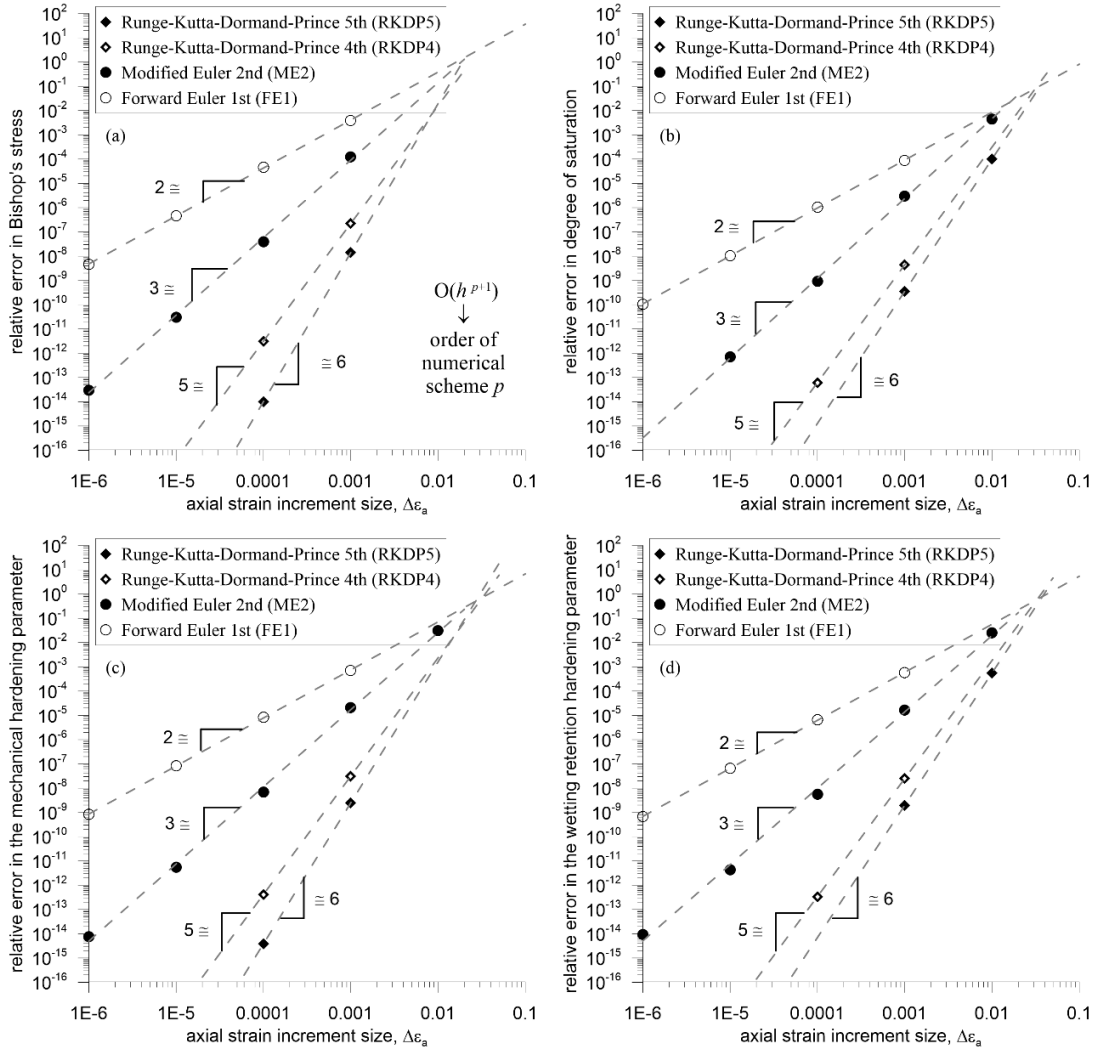
Figure 8. Relative error for single-step explicit integration schemes against axial strain increment size for a single elasto-plastic axial strain increment (at constant radial strain) under wetting: (a) Bishop's stress $\boldsymbol{\sigma}^*$; (b) degree of saturation S_r; (c) mechanical hardening parameter p_0'; (d) water retention hardening parameter s_{10}^*.

5.2. Substepping analysis: cumulative relative error

Once a substepping integration scheme has been verified at a single step level, the verification process should study the numerical performance over several substeps. In this context, Lloret-Cabot et al. (2016) propose to study the behaviour of the cumulative relative error E incurred in an integration scheme when the substepping is active. Assuming no cancellation, the addition of each amount of relative error e incurred in each substep corresponds to the cumulative relative error E. Lloret-Cabot et al. (2016) show that $e \cong ch^{p+1}$ (where h is the substep size, p is the order of the integration scheme

916 and c is simply a constant that fixes the position of an error line for a single step/substep

917 in the ln$e$:ln$h$ plane) and that, for n equal-sized substeps of size h, $E \cong nch^{p+1} = Hch^p$

918 (where H is the size of the total increment integrated i.e. $H=hn$). This means that the

919 final cumulative error (incurred during the integration of a given total increment H)

920 approximately lies on a straight line when plotted against the substep size h in a log-log

921 scale, having gradient 2 for the ME2 and 5 for RKDP5 with substepping schemes.

922 Similarly to the error lines for a single step/substep, the intercept of a cumulative error

923 line is Hc (as $E \cong Hch^p$) and, hence, the distance between the best-fitted straight line for

924 the single-step error and a cumulative error line for an increment involving many

925 substeps can be checked at a particular step/substep size h (Lloret-Cabot et al. 2016).

926 The numerical integration of Tests A and B is performed again using the ME2 and

927 RKDP5 schemes with substepping but now imposing values of $STOL$ small enough to

928 activate the substepping. In the analyses presented next, the maximum number of

929 substeps is limited to 10^{+06} and the values for $STOL$ vary from 1 to 10^{-08}.

930 The study of the numerical performance of each integration scheme is in two parts. An

931 investigation on how the errors are accumulated over the substeps integrated is

932 presented first, to check that the computed cumulative error is consistent with that of

933 the numerical method used. The performance maps proposed in Lloret-Cabot et al.

934 (2016) are presented in the second part of the analysis to check that the substepping

935 integration performs correctly. Without loss of generalisation, the first part of the

936 analysis is carried out only for Test A. The study of the performance maps, on the other

937 hand, is carried out for both numerical tests.

938 The different values of $STOL$ considered (from 1 to 10^{-08}) together with the accumulated

939 contributions of relative error at each substep are illustrated in Figures 9 and 10 for the

940 ME2 and RKDP5 schemes with substepping, respectively. Tables 7 and 8 present

941 typical values of cumulative relative error for ME2 and RKDP5 substepping schemes,

942 respectively, during the numerical integration of a volumetric strain increment of 0.1

943 for $STOL = 10^{-02}$, 10^{-04}, 10^{-06} and 10^{-08} (Test A). In the tables, the total number of

944 substeps required in the algorithm is indicated by TS whereas the total number of failed

945 substeps (substeps requiring a further subdivision in size) is indicated by TF. No drift

946 correction iterations were necessary in Test A.

947 Table 7. Typical cumulative relative error values in Bishop's stress $\boldsymbol{\sigma}^*$, degree of

948 saturation S_r, mechanical hardening parameter p_0' and wetting retention hardening

949 parameter s_{10}^* for an elasto-plastic isotropic strain increment of $\Delta\varepsilon_v = 0.1$ at constant

950 suction for the modified Euler with substepping (ME2) considering different values of

951 *STOL*.

| *STOL*	Error in $\boldsymbol{\sigma}^*$	Error in S_r	Error in p_0'	Error in s_{10}^*	TS	TF
$1\cdot10^{-02}$	$2.96\cdot10^{-04}$	$1.44\cdot10^{-06}$	$4.45\cdot10^{-03}$	$3.57\cdot10^{-03}$	11	2
$1\cdot10^{-04}$	$2.79\cdot10^{-06}$	$1.32\cdot10^{-08}$	$4.45\cdot10^{-05}$	$3.56\cdot10^{-05}$	114	3
$1\cdot10^{-06}$	$2.78\cdot10^{-08}$	$1.31\cdot10^{-10}$	$4.46\cdot10^{-07}$	$3.57\cdot10^{-07}$	1141	4
$1\cdot10^{-08}$	$2.78\cdot10^{-10}$	$1.31\cdot10^{-12}$	$4.46\cdot10^{-09}$	$3.57\cdot10^{-09}$	11416	5

952 Table 8. Typical cumulative relative error values in Bishop's stress $\boldsymbol{\sigma}^*$, degree of

953 saturation S_r, mechanical hardening parameter p_0' and wetting retention hardening

954 parameter s_{10}^* for an elasto-plastic isotropic strain increment of $\Delta\varepsilon_v = 0.1$ at constant

955 suction for the Runge-Kutta-Dormand-Prince with substepping (RKDP5) considering

956 different values of *STOL*.

STOL	Error in $\boldsymbol{\sigma}^*$	Error in S_r	Error in p_0'	Error in s_{10}^*	TS	TF
$1\cdot10^{-02}$	$6.94\cdot10^{-06}$	$5.30\cdot10^{-12}$	$1.33\cdot10^{-03}$	$1.06\cdot10^{-03}$	1	0
$1\cdot10^{-04}$	$3.95\cdot10^{-07}$	$1.22\cdot10^{-13}$	$8.87\cdot10^{-05}$	$7.10\cdot10^{-05}$	2	2
$1\cdot10^{-06}$	$1.07\cdot10^{-09}$	$1.24\cdot10^{-15}$	$2.72\cdot10^{-07}$	$2.17\cdot10^{-07}$	6	2
$1\cdot10^{-08}$	$8.38\cdot10^{-12}$	$1.24\cdot10^{-15}$	$2.16\cdot10^{-09}$	$1.73\cdot10^{-09}$	16	2

957 The form of plotting the results shown in Figures 9 and 10 is particularly convenient to

958 study how the cumulative relative error increases as the integration progresses

959 (indicated by a series of data points forming a near vertical path in the figure) for various

960 values of *STOL*. During a typical substepping integration of a prescribed volumetric

961 strain increment $\Delta\varepsilon_v$ with n substeps, the relative error incurred in each of these substeps

962 (all fulfilling the imposed *STOL*) accumulates over the substeps to give a value of the

963 cumulative relative error (Lloret-Cabot et al., 2016). Figures 9 and 10 demonstrate that,

964 indeed, the final values of cumulative relative error once the entire $\Delta\varepsilon_v$ has been

965 integrated approximately lie on a straight line of gradient two for the ME2 with

966 substepping and five for the RKDP5 with substepping (see dashed lines). This

967 behaviour is true for all values of *STOL* used (Figures 9 and 10). The vertical distance

968 (measured upwards) from the best-fitted straight line for the single substep relative error

969 (indicated by a thicker dark line) and one of these cumulative relative error lines (at a

970 particular total increment size $\Delta\varepsilon_v$ and substep size $\delta\varepsilon_v$) corresponds to $1/n$ where n is

971   the number of substeps (Lloret-Cabot et al., 2016). This error response is illustrated in

972   Figure 9 for three different sizes of volumetric strain increment (i.e. 0.001, 0.01 or 0.1),

973   when using the ME2 with substepping and a value of $STOL=10^{-08}$. A total number of

974   118 substeps are needed to integrate the volumetric strain increment size of 0.001, 1185

975   for 0.01 and 11416 for 0.1. This response is less apparent when using the RKDP5

976   scheme because of the small number of substeps typically required in this higher order

977   method (Figure 10).

978   During the numerical integration of each $\Delta\varepsilon_v$ considered, the actual substep size being

979   integrated is quite regular in the two substepping schemes considered as reflected by

980   the approximately vertical paths traced by the cumulative error (Figures 9 and 10).
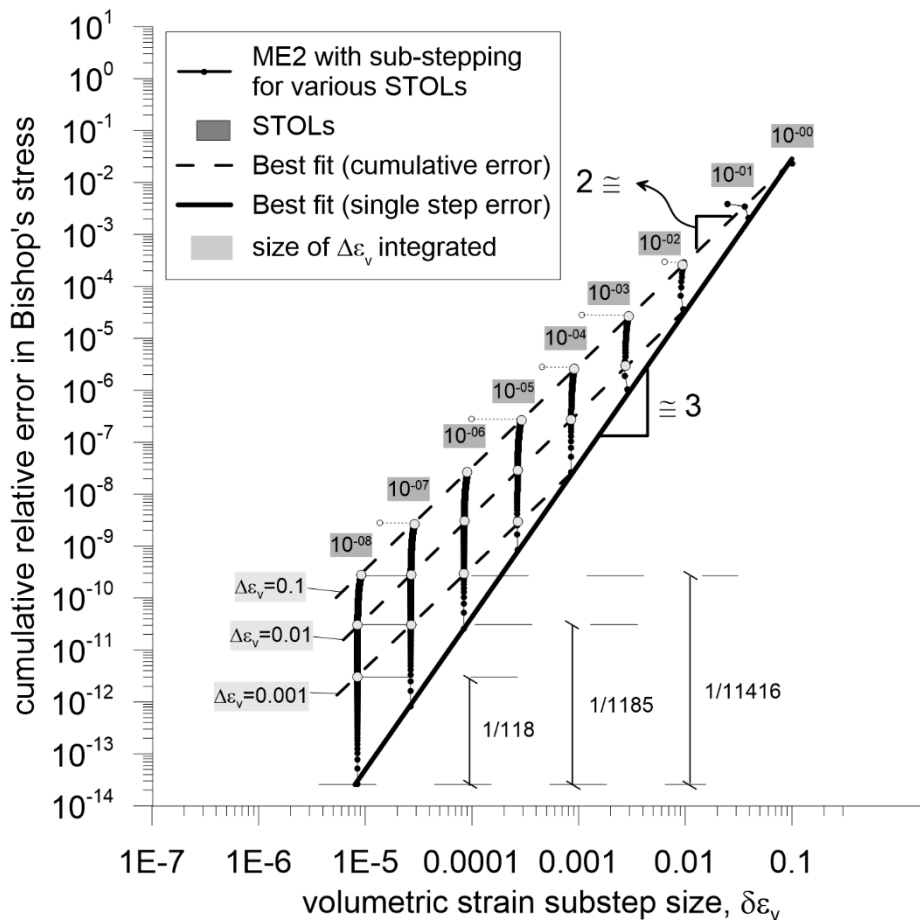
981

982   Figure 9. Cumulative relative error behaviour in Bishop's stresses for the modified

983   Euler with substepping (ME2) integration scheme with different values of *STOL* against

984   strain increment size for an elasto-plastic isotropic loading increment.
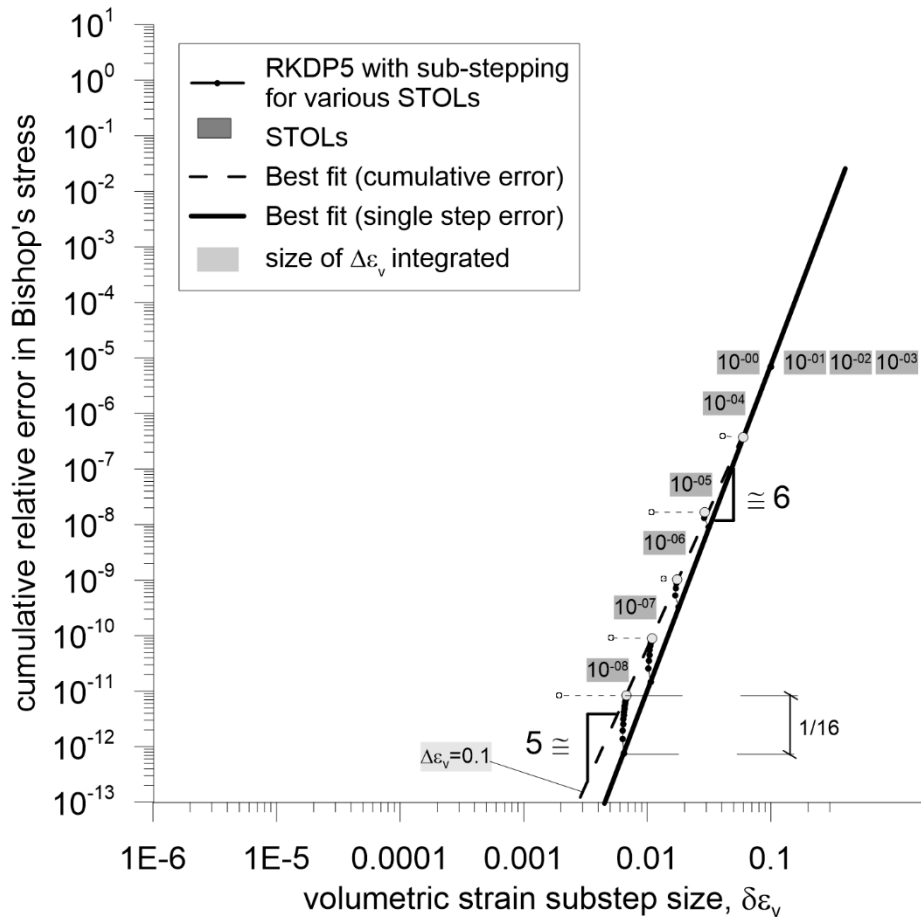
Figure 10. Cumulative relative error behaviour in Bishop's stresses for the Runge-Kutta-Dormand-Prince with substepping (RKDP5) integration scheme with different values of *STOL* against strain increment size for an elasto-plastic isotropic loading increment.

Figure 11 shows the cumulative relative error (i.e. the accumulated relative error incurred over the number of substeps required to integrate a given increment of volumetric strain) for Bishop's stresses incurred in Test A plotted against *STOL* for each integrated size of volumetric strain increment $\Delta\varepsilon_v$. Figure 12 plots the same cumulative relative error plotted against the number of substeps required for the integration of the entire strain increment. In these figures, part a) presents the results for the ME2 with substepping and part b) their RKDP5 substepping counterparts.

Inspection of Figure 11 shows how the influence of *STOL* in the relative error incurred in an individual substep $\delta\varepsilon_v$ affects the cumulative relative error incurred in the integration of the entire $\Delta\varepsilon_v$. As expected, a reduction in the values of *STOL* leads to a reduction in the relative error incurred in each individual substep of the computations

which, in turn, reduces the cumulative relative error. However, this reduction of the cumulative relative error with decreasing *STOL* is not apparent for small sizes of volumetric strain increment unless *STOL* is less than a critical size (Figure 11). Similarly to what is observed in saturated soils (Lloret-Cabot et al., 2016), this is because for small increment sizes, even without substepping the difference between the two solutions of different order within the substepping scheme tends to be very small and, if it is less than the *STOL* considered, the substepping strategy is not activated. For example, for a volumetric strain increment size of 10^{-02}, values of *STOL* smaller than 10^{-02} are required to activate the substepping strategy with the ME2 scheme (Point Y in Figure 11a). The RKDP5 with substepping, on the other hand, needs values of *STOL* smaller than 10^{-06} to activate substepping for a volumetric strain increment size of 10^{-2} (Point Y in Figure 11b). Figure 11a shows that for a volumetric strain increment size of 10^{-02}, 1186 substeps are required in the ME2 substepping scheme (with $STOL = 10^{-08}$) to reach a cumulative relative error of about 10^{-10}. In contrast, the RKDP5 substepping scheme requires only 2 substeps to reach a similar (even substantially smaller) value of the cumulative relative error (see Figure 11b).

As discussed earlier, the second order accurate modified Euler with substepping uses $r \cong 0.9(STOL/REL_n)^{1/2}$ and the fifth order accurate Runge-Kutta-Dormand-Prince with substepping uses $r \cong 0.9(STOL/REL_n)^{1/5}$. This means that the variation of the cumulative relative error with the number of substeps should follow, approximately, straight lines of gradient -2 for the ME2 integration scheme and, similarly, approximately straight lines of gradient -5 for the RKDP5 integration scheme as correctly illustrated in Figure 12.

The plots presented in Figure 11 and 12 correspond to the performance maps proposed in Lloret-Cabot et al. (2016) for saturated soils and its application is demonstrated here for unsaturated soils. The results obtained confirm that this specific form of plotting the computational outcomes from a substepping integration scheme is a powerful verification tool.

Similar error responses to those just discussed for Figure 12 are also observed in Figure 13 (Test B) for σ^*, S_r, p_0' and s_{10}^* when using the ME2 substepping integration scheme. Even in the case of not using an analytical solution to compute the relative error, the

1032 error behaviour observed is consistent with that discussed when analytical solutions
1033 were available.
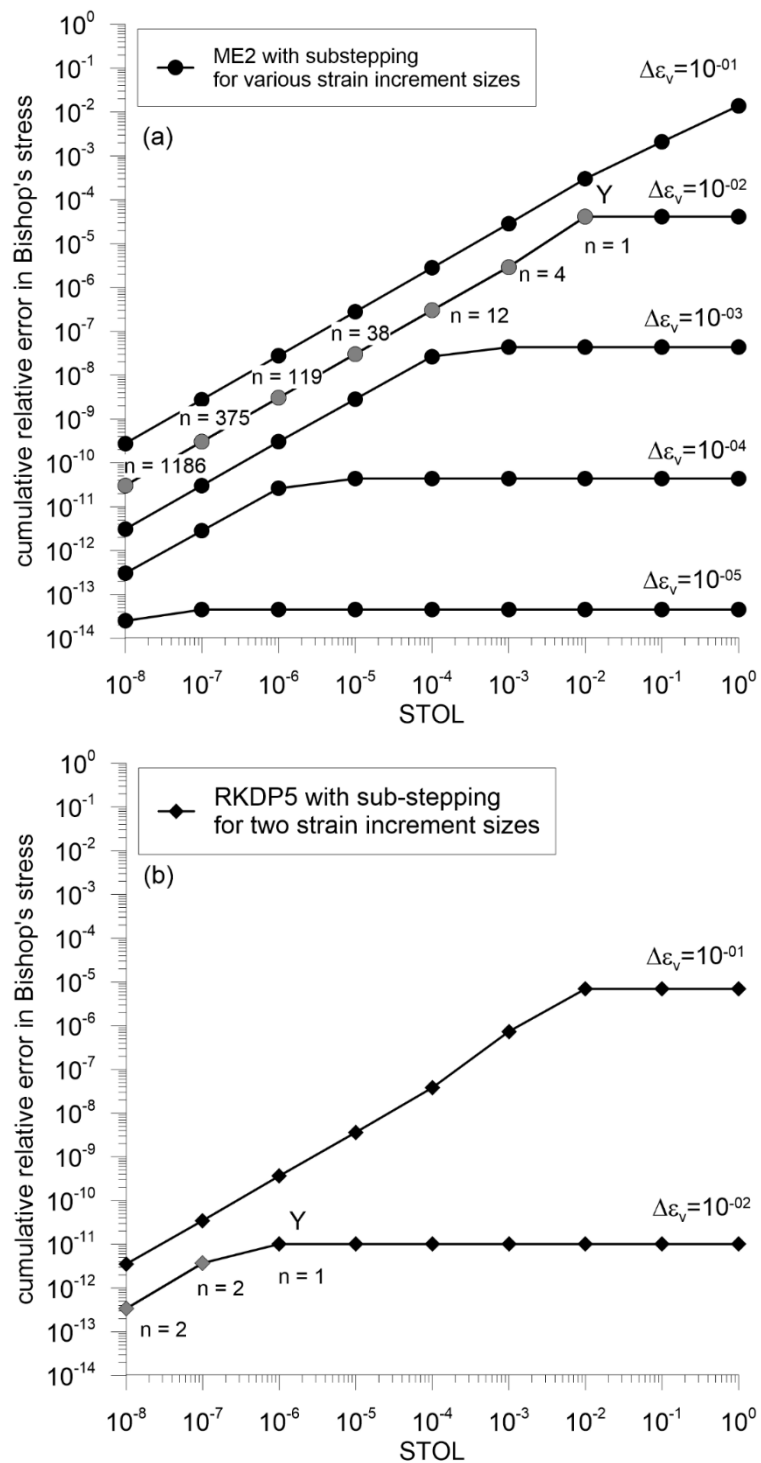
1034 Figure 11. Cumulative relative error behaviour against *STOL* for an elasto-plastic
1035 isotropic strain increment at constant suction: (a) Modified Euler with substepping
1036 scheme (ME2); (b) Runge-Kutta-Dormand-Prince with substepping scheme (RKDP5).
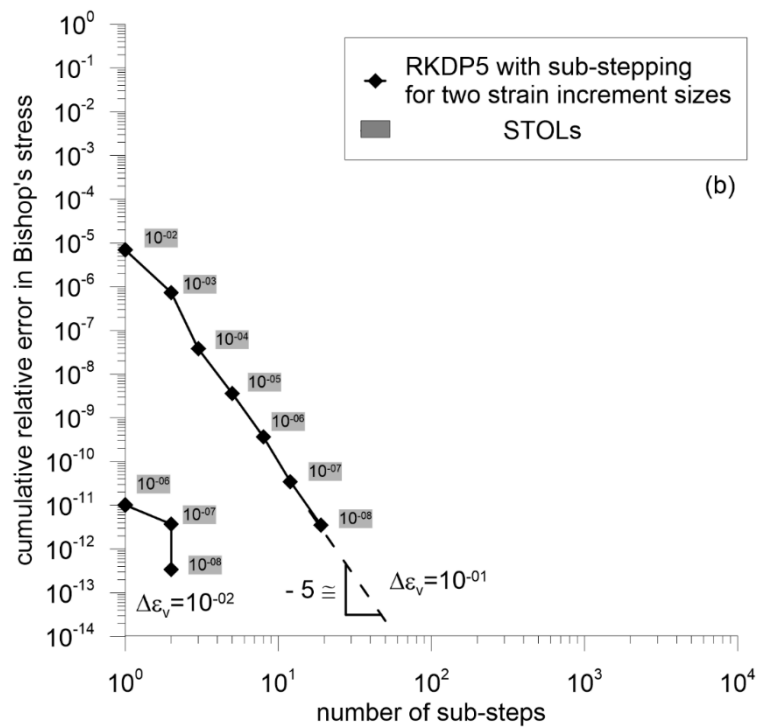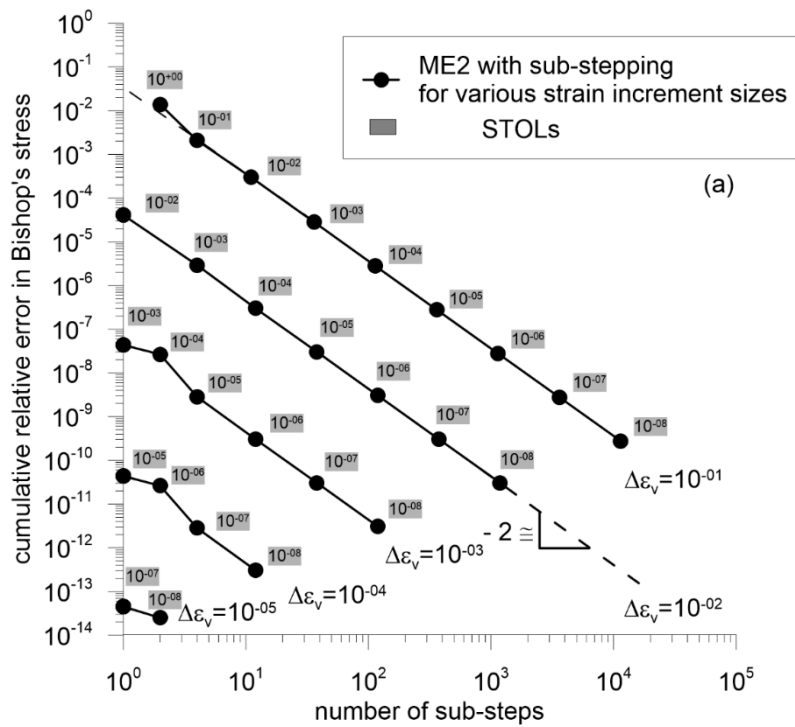
Figure 12. Cumulative relative error behaviour against number of substeps for an elasto-plastic isotropic strain increment at constant suction: (a) Modified Euler with substepping scheme (ME2); (b) Runge-Kutta-Dormand-Prince with substepping scheme (RKDP5).
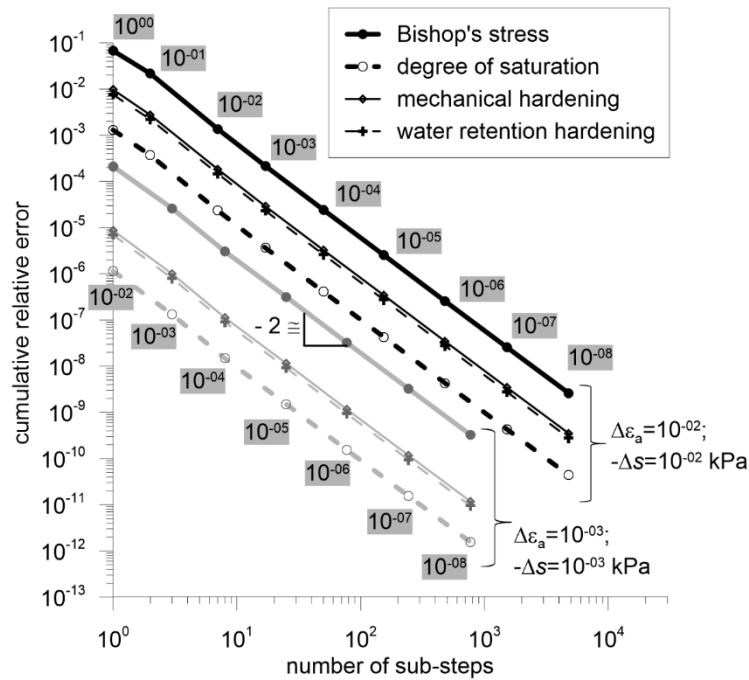
1041

Figure 13. Cumulative relative error behaviour against number of substeps for an elasto-
plastic axial strain increment (at constant radial strain) under wetting using the modified
Euler with substepping scheme (ME2).

5.3. Computational cost and efficiency

The simplicity of the numerical examples discussed above implies a very small CPU
time and, therefore, it is reasonable to assess the computational cost associated with
each example as proportional to the number of evaluations of the constitutive relations
that the substepping integration scheme employs to solve the problem (Sloan et al.,
2001). Equivalently to Lloret-Cabot et al. (2016), two evaluations of the constitutive
relations are required in the ME with substepping scheme and six are needed in the
RKDP substepping scheme. Additionally, the computational cost associated with any
rejected step as well as the computational cost associated with the number of iterations
used by the drift correction subroutine are also accounted for.

Figure 14 shows the computational cost as a function of $STOL$ (i.e. $STOL= 10^{-02}$, 10^{-04},
10^{-06} and 10^{-08}), and the input increment size for the three numerical tests considered
earlier. Plots on the left correspond to the ME substepping scheme and plots on the right
show the approximations for the RKDP substepping scheme. A similar pattern to that

found by Lloret-Cabot et al. (2016) when using the MCC model is also observed here for the GCM. In general, from the two integration schemes investigated, the ME substepping scheme requires a larger number of evaluations of the constitutive relations (i.e. higher computational cost) to satisfy the value of *STOL* when the sizes of the input increment $\Delta\varepsilon_v$, $\Delta\varepsilon_a$, or Δs are large (and this observation is more pronounced when the values of *STOL* are more restrictive). In contrast, the RKDP substepping scheme is more expensive for the smaller increment sizes. For intermediate increment sizes, the optimal computational efficiency depends on the level of accuracy specified (RKDP substepping scheme is most efficient for stringent tolerances whereas ME substepping scheme is best for looser values of *STOL*).
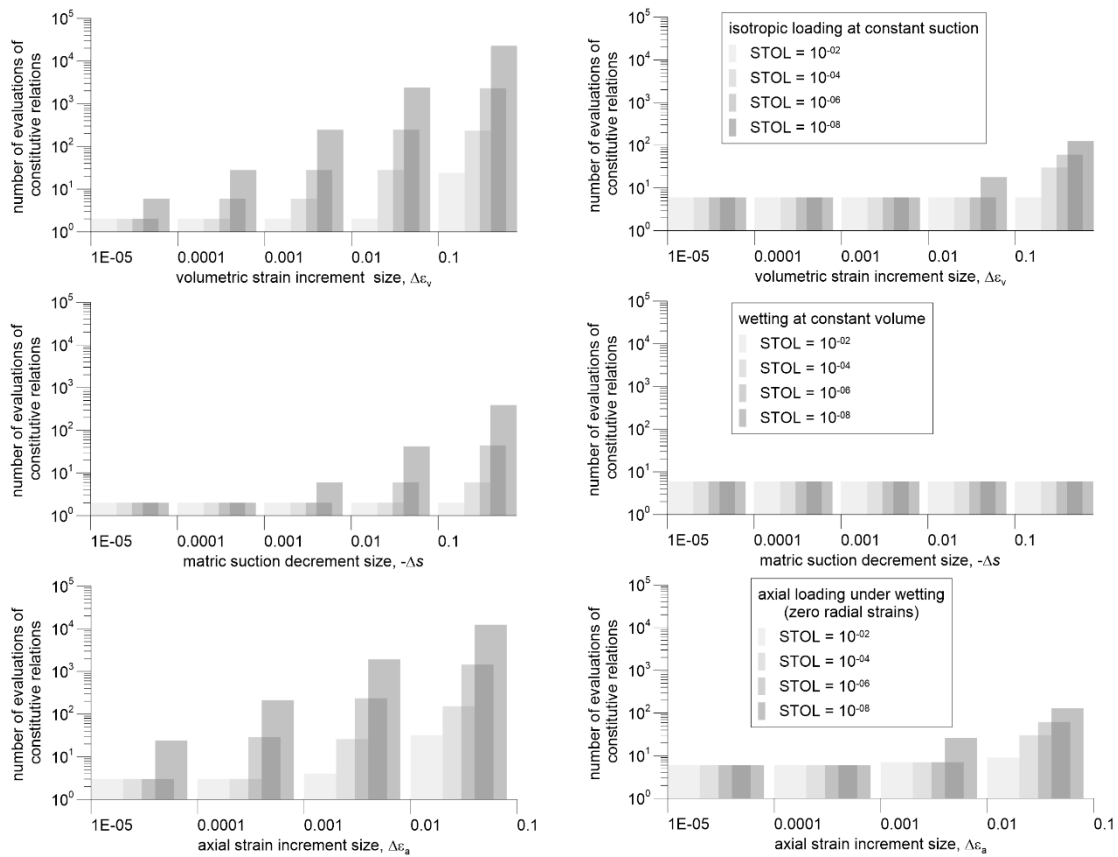
Figure 14. Computational cost for different STOL values against input increment sizes: (left) modified Euler substepping scheme; (right) Runge-Kutta-Dormand-Prince substepping scheme.

6. CONCLUSIONS

The complete formulation of the incremental constitutive relations of the Glasgow Coupled Model (GCM) has been presented for all possible elastic and elasto-plastic responses of the model, including transitions between saturated and unsaturated conditions. The formulation is expressed in terms of the increments of strain and increments of suction (i.e. strain-driven formulation) so that it is suitable for implementation into a finite element program, as it properly defines an initial value problem (IVP) when the initial stress state and the increments of strain and suction are known.

A rigorous algorithm capable of identifying unambiguously which is the model response activated by a trial stress path has been developed after a small reformulation of the GCM that included the derivation of a useful closed-form expression for the mechanical yield curve in terms of degree of saturation. The correct identification of the intersection point, when a trial stress path moves from elastic to elasto-plastic behaviour, is achieved by using the Pegasus algorithm, widely used for solving the equivalent problem in explicit formulations for saturated soil models. The same strategy is applied to find the correct stress point at saturation and desaturation. A drift correction subroutine has been also presented to correct any potential deviation of the stress point at the end of each integrated elasto-plastic step/substep.

Two explicit substepping formulations to integrate numerically the IVP defined by the initial state and the incremental relations of the GCM have been then presented, extending to unsaturated conditions the well-known explicit substepping integration schemes with automatic error control for saturated soils. These two substepping schemes presented correspond to the second order accurate modified Euler with substepping and the fifth order accurate Runge-Kutta-Dormand-Prince with substepping.

In contrast to existing substepping formulations with automatic error control for saturated soils, which account only for the relative error associated with the integration of the mechanical part of the problem (i.e. stresses and mechanical hardening parameter), the extended substepping version with automatic error control presented in this paper accounts for the relative error incurred during the numerical integration of both the mechanical (stresses and mechanical hardening parameter) and water retention (degree of saturation and water retention hardening parameter) components of the

1106   problem. This is essential when applying substepping schemes to solve problems
1107   involving unsaturated soils, as this is what ensures an accurate and efficient integration.

1108   The correctness of the two substepping schemes presented is checked by investigating
1109   how the error over an individual step/substep and the cumulative error over multiple
1110   substeps propagate during the integration of two simple numerical tests, involving an
1111   isotropic straining at constant suction and a combined axial straining under wetting.
1112   The behaviour of the relative error observed when adopting a single-step integration in
1113   solving each of these tests is different for the mechanical and the water retention
1114   components of the problem, which confirms the importance of accounting separately
1115   for the different sources of error. The computational performance of the two
1116   substepping schemes is then checked by ensuring that the influence of the internal
1117   substepping tolerance *STOL* on the accuracy and the number of substeps used is as
1118   expected. The results obtained extend to unsaturated conditions the conclusions
1119   observed for saturated soils (Lloret-Cabot et al., 2016), confirming that the substepping
1120   methods proposed are capable of controlling the cumulative error (i.e. they satisfy the
1121   error tolerance *STOL* for all the cases considered).

1122   Finally, this investigation confirms that the importance of updating rigorously the
1123   specific volume in Cam Clay family models for saturated soils in substepping
1124   integration schemes extends also to the rigorous update of the degree of saturation in
1125   substepping integration schemes for critical state models for unsaturated soils.

1126   7. ACKNOWLEDGEMENTS

1130   8. APPENDICES

1131   8.1 Appendix A

1132   The Glasgow Coupled Model (GCM) predicts that isotropic stress states at the
1133   intersection of f_M and f_{WR} yield curves fall on unique unsaturated isotropic normal
1134   compression planar surfaces for v (in $v : \ln p^* : \ln s^*$ space) and also for S_r (in $S_r : \ln p^*$

1135 $: \ln s^*$ space). The forms of these two planar surfaces are (see also Lloret-Cabot et al.

1136   2017):

1137 $$v = N^* - \lambda^* \ln p_0^* + k_1^* \ln s_1^*$$ (A1)

1138 $$S_r = \Omega^* - \lambda_s^* \ln s_1^* + k_2^* \ln p_0^*$$ (A2)

1139   where N^* and Ω^* are their respective intercepts. The expressions of gradients λ^*, k_1^*,

1140 λ_s^* and k_2^* are a combination of the soil parameters of the model (assuming $\mathrm{d}S_r^e = 0$):

1141 $$\lambda^* = \frac{\lambda - k_1 k_2 \kappa}{1 - k_1 k_2}$$ (A3)

1142 $$k_1^* = k_1 \frac{\lambda - \kappa}{1 - k_1 k_2}$$ (A4)

1143 $$\lambda_s^* = \frac{\lambda_s}{1 - k_1 k_2}$$ (A5)

1144 $$k_2^* = k_2 \frac{\lambda_s}{1 - k_1 k_2}$$ (A6)

1145   Assuming $\kappa_s = 0$ (the gradient of elastic scanning curves in the $S_r:\ln s^*$ plane as defined

1146   in Wheeler et al., 2003), Lloret-Cabot et al. (2017) derives the following relationship

1147   between intercepts N, N^* and Ω^*:

1148 $$\Omega^* = 1 - \frac{\left(N^* - N\right)\lambda_s}{k_1 \left(\lambda - \kappa\right)}$$ (A7)

1149   Combining the above equations with the elastic relations of the GCM, it is possible to

1150   find the following expressions for v for any general stress state (Lloret-Cabot et al.,

1151   2017):

1152 $$v = N^* - \lambda^* \ln p_0^* + k_1^* \ln s_1^* + \kappa \ln\left(\frac{p_0^*}{p^*}\right)$$ (A8)

1153   Equation A8 can be used to calculate initial value of v when initial values of p^*, p_0^* and

1154 s_1^* are known, together with the model parameters. Given that $dS_r^e = 0$, the initial value

1155   of S_r can be also calculated from Equation A2 (Lloret-Cabot et al., 2017).

1156   8.2 Appendix B

1157   A more formalised description of the sequence of the steps followed by the algorithm

1158   to determine which is the active response of the GCM is presented here for the most

1159   general case of a stress point starting inside the three yield curves of the model and

1160   potentially activating any of the six possible model responses. Any other case (i.e. stress

1161   point starting on one or two yield curves) is a particular case of this one.

1162   (A) Compute *trial 1* assuming purely elastic behaviour.

1163   If *trial 1* is inside f_M, f_{DR} and f_{WR} then, elastic update from i to $i+1$ and *return*.

1164   If *trial 1* is outside f_M, outside f_R or outside both, yielding has occurred (note that

1165 f_R is either f_{DR} or f_{WR}). Hence:

1166   If *trial 1* is outside only one yield curve (f_M or f_R).

1167   Find the portion α of $\Delta\boldsymbol{\varepsilon}$ and Δs, that moves the stress point to the

1168   intersection with f_M, i_{M1}, (or with f_R, i_{R1}). Note that $\alpha = 0$ means that the

1169   stress point was already on f_M (or f_R).

1170   Update elastic from i to i_{M1} (or i_{R1}).

1171   Move to *trial 2* with the portion not yet integrated of $\Delta\boldsymbol{\varepsilon}$ and Δs given by

1172 $(1-\alpha)$. At this stage, the stress point is on f_M (or on f_R).

1173   If *trial 1* is outside two yield curves (f_M and f_R).

1174   Find intersection with f_M, α_1.

1175   Find intersection with f_R, α_2.

1176   If $\alpha_1 < \alpha_2$ then f_M is reached first.

1177   Update elastic from i to i_{M1} using α_1.

1178   Move to *trial 2* with $(1-\alpha_1)$. The stress point is on f_M

1179   If $\alpha_2 \leq \alpha_1$ then f_R is reached first.

1180   Elastic update from i to i_{R1} using α_2 (note that if $\alpha_1 = \alpha_2$, then $i_{R1}=i_{M1}$

1181   and, hence, $\alpha_1 = \alpha_2 = 0$ i.e. stress point is on both f_M and f_R)

1182   Move to *trial 2* with $(1-\alpha_2)$. The stress point is on f_R (if $\alpha_2 < \alpha_1$) or

1183   on both f_R and f_M (if $\alpha_2 = \alpha_1$).

1184 (B) At this stage, there are three possible ways to compute *trial 2* depending on whether

1185 the stress point is on f_M (point i_{M1}, case B.1) on f_R (point i_{R1}, case B.2) or on both (point

1186 i_Y, case B.3).

1187 (B.1) If the stress point is only on f_M (point i_{M1}) then,

1188 Compute *trial 2* assuming yielding on f_M, but not on f_R (using the portion not yet

1189 integrated of $\Delta\boldsymbol{\varepsilon}$ and Δs i.e. $(1-\alpha)$ if *trial 1* crosses only one yield curve or $(1-\alpha_1)$ if *trial*

1190 *1* crosses two yield curves).

1191   If *trial 2* is inside f_R, then yielding on f_M (but not on f_R) has occurred.

1192   Update stress point from i_{M1} to $i_{M1}+1$ assuming yielding on f_M alone (using

1193 $1-\alpha$ or $1-\alpha_1$) and *return*.

1194   If *trial 2* is outside f_R, then *trial 2* crosses f_R at point i_Y, on both f_M and f_R.

1195   Find intersection with f_R $i_R = i_Y$, β. Note that $\beta = 0$ means that the stress

1196   point was already on f_R.

1197   Update stress point from i_{M1} to i_R assuming yielding on f_M alone (using β)

1198   and move to *trial 3*.

1199 At this stage, the stress point is on f_M and f_R (point i_Y). There are only two possible

1200 model responses here: yielding on only f_R or simultaneous yielding on f_M and f_R.

1201 Yielding on only f_M is not possible because, if that was the case, *trial 2* would had fallen

1202 inside f_R when assuming yielding on only f_M and, in fact, the algorithm is at this point

1203 because *trial 2* fell outside f_R.

1204 Compute *trial 3* assuming yielding on f_R (but not on f_M) with $(1-\beta)$.

1205   If *trial 3* is inside f_M, then update the stress point from i_Y to i_Y+1 assuming

1206   yielding on f_R alone (using $1-\beta$) and *return*.

1207   Otherwise, update the stress point from i_Y to i_Y+1 assuming simultaneous yielding

1208   on f_M and f_R (using $1-\beta$) and *return*.

1209 (B.2) If the stress point is on f_R (point i_{R1}) then,

1210 Compute *trial 2* assuming yielding on f_R (but not on f_M) using the portion not yet

1211 integrated of $\Delta\boldsymbol{\varepsilon}$ and Δs i.e. $(1-\alpha)$ or $(1-\alpha_2)$.

1212   If *trial 2* is inside f_M, then yielding on f_R (but not on f_M) has occurred

1213   Update stress point from i_{R1} to $i_{R1}+1$ assuming yielding on f_R alone (using

1214 $1-\alpha$ or $1-\alpha_2$) and *return*.

1215   If *trial 2* is outside f_M, then *trial 2* crosses f_M at point i_Y, on both f_M and f_R.

1216   Find intersection with f_M $i_M = i_Y$, β.

1217   Update stress point from i_R to i_M assuming yielding on f_R alone (using β)

1218   and move to *trial 3*.

1219   At this stage, the stress point is on f_M and f_R (point i_Y). There are only two possible

1220   model responses here: yielding on only f_M or simultaneous yielding on f_M and f_R. Note

1221   that yielding on only f_R is not possible because, if that was the case, *trial 2* would had

1222   fallen inside f_M when assuming yielding on only f_R and, in fact, fell outside f_M.

1223   Compute *trial 3* assuming yielding on f_M (but not on f_R) with (1-β).

1224   If *trial 3* is inside f_R, then update the stress point from i_Y to i_Y+1 assuming yielding

1225   on f_M alone (using 1-β) and *return*.

1226   Otherwise, update the stress point from i_Y to i_Y+1 assuming simultaneous yielding

1227   on f_M and f_R (using 1-β) and *return*.

1228   (B.3) If the stress point is on f_M and f_R (point i_Y). There are three possible model

1229   responses here: yielding on only f_R, yielding on only f_M or simultaneous yielding on f_M

1230   and f_R. Therefore, the algorithm may need to compute a maximum of two trials to ensure

1231   the correct model response.

1232   Compute *trial 2* assuming yielding on f_R, (but not on f_M) using the portion not yet

1233   integrated of $\Delta\boldsymbol{\varepsilon}$ and Δs i.e. (1-α) or (1-α_2).

1234   If *trial 2* is inside f_M, then yielding on f_R (but not on f_M) has occurred.

1235   Update from i_Y to i_Y+1 assuming yielding on f_R alone (using 1-α or 1-α_2)

1236   and *return*.

1237   Otherwise, move to *trial 3*.

1238   Compute *trial 3* assuming yielding on f_M (but not on f_R) using the portion not yet

1239   integrated of $\Delta\boldsymbol{\varepsilon}$ and Δs i.e. (1-α) or (1-α_2).

1240   If *trial 3* is inside f_R, then update the stress point from i_Y to i_Y+1 assuming yielding

1241   on f_M alone and *return*.

1242   Otherwise, update the stress point from i_Y to i_Y+1 assuming simultaneous yielding

1243   on f_M and f_R and *return*.

1244   Note that step (B.3) can be accommodated in steps (B.1) or (B.2), but, for clarification,

1245   it has been kept as a separate case.

1246   8.3 Appendix C

1247   Given the increments of $\Delta\boldsymbol{\varepsilon}$ and Δs, the stress state can move from elastic to elasto-

1248   plastic. In the context of the GCM, this means that a *trial* intersects at least one yield

1249   curve and that an intersection point needs to be found. The proposed integration

1250   schemes solve all intersections using the Pegasus algorithm illustrated in Figure C1

1251   (Dowell and Jarratt, 1972). Two conditions are necessary for a *trial* to cross a generic

1252   yield curve f_A. The first one is that the stress point at i is not already lying on f_A

1253   (indicated in Figure C1 as $^0f_A < \text{-}FTOL$). The second one is that the evaluation of the

1254   yield curve at the *trial* is larger than *FTOL* (indicated by $^1f_A > FTOL$ in Figure C1). If

1255   both of these conditions are true, the Pegasus algorithm finds the scalar α that defines

1256   the portion of $\Delta\boldsymbol{\varepsilon}$ and Δs that moves the current stress point to f_A (indicated as i in Figure

1257   C1). A value of α = 0 indicates that the initial stress point is already on f_A (i.e. $|f_A| \leq$

1258   *FTOL*) and the update of the stress point is elasto-plastic. A value α = 1 indicates that

1259   the final stress point (once the full size of $\Delta\boldsymbol{\varepsilon}$ and Δs has been updated) ends up exactly

1260   on f_A so that no intersection occurs. These two extreme cases explain why the possible

1261   values of the scalar α range between 0 and 1.

$$\textbf{\textit{if}}\left(^{1}f_{A} > FTOL\right)\textbf{\textit{then}} \qquad !^{1}f_{A} \text{ corresponds to } {}^{trial}f_{A}$$

$$\textbf{\textit{if}}\left(^{0}f_{A} < -FTOL\right)\textbf{\textit{then}} \quad !^{0}f_{A} \text{ corresponds to } {}^{i}f_{A}$$

$$\alpha_{0} = 0$$
$$\alpha_{1} = 1$$
GO TO **1**

$\qquad$ **endif**

! stress point on f_{A} at i

$$\alpha = 0$$
$\qquad$ GO TO **3**

1 *continue*

! Find the elastic portion α of $(\Delta\boldsymbol{\varepsilon}, \Delta s)$ that moves the stress point to $^{0}f_{A}$

$\quad$ **do 2** $n = 1$, maxit $\qquad$! maxit is the maximum number of iterations

$$\alpha = \alpha_{1} - \left(\alpha_{1} - \alpha_{0}\right){}^{1}f_{A}\Big/\left(^{1}f_{A} - {}^{0}f_{A}\right)$$

$^{t}\Delta\boldsymbol{\varepsilon} = \alpha\Delta\boldsymbol{\varepsilon}$ and $^{t}\Delta s = \alpha\Delta s$

update with $^{t}\Delta\boldsymbol{\varepsilon}$ *and* $^{t}\Delta s$

$\quad f_{A} \qquad\qquad$! Evaluation of f_{A} at the updated point

$\quad$ **if**$\left(\left|f_{A}\right| \leq FTOL\right)$**then**

$\qquad$ GO TO **3**

$\quad$ **endif**

$\quad$ **if**$\left(^{0}f_{A} \cdot f_{A} > 0\right)$**then**

$$^{1}f_{A} = {}^{1}f_{A} \cdot {}^{0}f_{A}\Big/\left(^{0}f_{A} + f_{A}\right)$$

$\quad$ **else**

$$\alpha_{1} = \alpha_{0}$$
$$^{1}f_{A} = {}^{0}f_{A}$$

$\quad$ **endif**

$$\alpha_{0} = \alpha$$
$$^{0}f_{A} = f_{A}$$

$\quad$ **endo**

2 *continue*

STOP $\qquad\qquad\qquad$!Algorithm stops (too many iterations)

3 *continue*

endif

Figure C.1 Typical intersection problem using Pegasus algorithm (Dowell and Jarratt, 1972)

9. REFERENCES

55

1267 1.Abbo AJ. Finite element algorithms for elastoplasticity and consolidation. PhD thesis,
1268   University of Newcastle, Australia, (1997).

1269 2.Alonso EE, Gens A, Josa A. A constitutive model for partially saturated soils.
1270   Géotechnique, 40(3) (1990), pp. 405–430.

1271 3.Borja RI, White JA. Continuum deformation and stability analyses of a steep hillside
1272   slope under rainfall infiltration. Acta Geotech, 5 (2010), pp. 1–14.

1273 4.Cattaneo F, Vecchia GDella, Jommi C. Evaluation of numerical stress-point
1274   algorithms on elastic–plastic models for unsaturated soils with hardening dependent
1275   on the degree of saturation. Computers and Geotechnics, 55 (2014), pp. 404–415.

1276 5.Dormand JR, Prince PJ. A family of embedded Runge-Kutta formulae. Journal of
1277   Computational and Applied Mathematics, 6(1) 1980, pp. 19–26.

1278 6.Dowell M, Jarratt P. The Pegasus method for computing the root of an equation, BIT,
1279   12 (1972), pp. 503–8.

1280 7.Gallipoli D, Gens A, Sharma R, Vaunat J. An elasto-plastic model for unsaturated
1281   soil incorporating the effects of suction and degree of saturation on mechanical
1282   behaviour. Géotechnique, 53(1) (2003), pp. 123–136.

1283 8.Gens A. Soil–environment interactions in geotechnical engineering. Géotechnique,
1284   60(1) (2010), pp. 3–74.

1285 9.Houlsby GT. The work input to an unsaturated granular material. Géotechnique, 47(1)
1286   (1997), pp. 193–196.

1287 10.Jommi C, Di Prisco C. A simple theoretical approach for modelling the mechanical
1288   behaviour of unsaturated granular soils (in Italian) Il ruolo dei fluidi in ingegneia
1289   geotecnica. Proc. of Italian conf. Mondovi, (1994), pp. 167–188.

1290 11. Khalili N., Habte M.A., & Zargarbashi S. A fully coupled flow deformation model
1291   for cyclic analysis of unsaturated soils including hydraulic and mechanical hysteresis
1292   Comp. Geotech., 35(6) (2008), pp. 872–889.

1293 12.Lloret-Cabot M, Sánchez M, Wheeler SJ. Formulation of a three-dimensional
1294   constitutive model for unsaturated soils incorporating mechanical-water retention
1295   couplings. International Journal for Numerical and Analytical Methods in
1296   Geomechanics, 37 (2013), pp. 3008–3035.

1297 13.Lloret-Cabot M, Sloan SW, Sheng D, Abbo AJ. Error behaviour in explicit
1298   integration algorithms with automatic substepping. International Journal for
1299   Numerical Methods in Engineering, 108(9) (2016), pp. 1030–1053.

1300   14. Lloret-Cabot M, Wheeler SJ, Pineda JA, Romero E, Sheng D. From saturated to
1301   unsaturated conditions and vice versa. Acta Geotech., 13(1) (2018a), pp. 15–37.

1302   15. Lloret-Cabot M, Wheeler SJ, Pineda JA, Romero E, Sheng D. Reply to Discussion
1303   of "From saturated to unsaturated conditions and vice versa". Acta Geotech., 13(2)
1304   (2018b), pp. 493–495.

1305   16. Lloret-Cabot M, Wheeler SJ, Sánchez M. A unified mechanical and retention model
1306   for saturated and unsaturated soil behaviour. Acta Geotech., 12(1) (2017), pp. 1–
1307   21.

1308   17. Lloret-Cabot M, Wheeler SJ, Sánchez M. Unification of plastic compression in a
1309   coupled mechanical and water retention model for unsaturated soils. Can. Geotech.
1310   J., 51(12) (2014), pp. 1488–1493.

1311   18. Lloret-Cabot M, Wheeler, SJ. The mechanical yield stress in unsaturated and
1312   saturated soils. Proc. 7th Int. conf. unsat. soils (eds W.W. Ng, A.K. Leung, A.C.F.
1313   Chiu, C. Zhou), Hong Kong, HKUST, (2018), pp. 221-226.

1314   19. Ng CWW, Pang, YW. Influence of stress state on soil-water characteristics and
1315   slope stability. J. Geotech. Eng. ASCE, 126(2) (2000), pp. 157–166.

1316   20. Nuth M. Laloui L. Advances in modelling hysteretic water retention curve in
1317   deformable soils. Comp. Geotech., 35(6) (2008), 835–844.

1318   21. Olivella S, Gens A, Carrera J, Alonso EE. Numerical formulation for a simulator
1319   (CODE_BRIGHT) for the coupled analysis of saline media. Engineering
1320   Computations, 13(7): (1996), pp. 87–112.

1321   22. Pedroso DM, Sheng D, Sloan, SW. Stress update algorithm for elastoplastic models
1322   with nonconvex yield surfaces. International Journal for Numerical Methods in
1323   Engineering, 76 (2008), pp. 2029–2062.

1324   23. Pérez-Foguet A, Rodríguez-Ferran A, Huerta A. Consistent tangent matrices for
1325   substepping schemes, Computer Methods in Applied Mechanics and Engineering,
1326   190(35-36) (2001), pp. 4627–4647.

1327   24. Pinyol NM, Alonso EE, Olivella, S. Rapid drawdown in slopes and embankments.
1328   Water Resources Research, 44(5) 2008, pp. 1–22.

1329   25. Potts DM, Gens A. A critical assessment of methods of correcting for drift from the
1330   yield surface in elastoplastic finite element analysis. International Journal for
1331   Numerical and Analytical Methods in Geomechanics, 9 (1985), pp. 149–59.

1332 26. Potts DM, Gens A. The effect of the plastic potential in boundary value problems
1333   involving plane strain deformation. International Journal for Numerical and
1334   Analytical Methods in Geomechanics, 8(3) (1984), 259–286.
1335 27. Potts DM, Zdravkovic L. Finite element analysis in geotechnical engineering:
1336   theory, (1999). Thomas Telford, London.
1337 28. Romero E, Gens A, Lloret A. Water permeability, water retention and
1338   microstructure of unsaturated compacted Boom clay. Eng. Geol., 54 (1999), pp.
1339   117–127.
1340 29. Roscoe KH, Burland JB. On the generalised stress-strain behavior of wet clay.
1341   Engineering Plasticity (eds Heyman J & Leckie FA), Cambridge University Press,
1342   Cambridge, (1968), pp. 535–609.
1343 30. Sánchez M, Gens A, Guimarães L, Olivella S. Implementation algorithm of a
1344   generalised plasticity model for swelling clays. Computers Geotechnics, 35(6)
1345   (2008), pp. 860–871.
1346 31. Shampine LF. Numerical Solution of Ordinary Differential Equations. Chapman &
1347   Hall, London, (1994).
1348 32. Sheng D, Sloan SW, Gens A, Smith DW. Finite element formulation and algorithms
1349   for unsaturated soils. Part I: Theory. International Journal for Numerical and
1350   Analytical Methods in Geomechanics, 27 (2003a), pp. 745–765.
1351 33. Sheng D, Sloan SW, Gens A, Smith DW. Finite element formulation and algorithms
1352   for unsaturated soils. Part II: Verification and Application. International Journal for
1353   Numerical and Analytical Methods in Geomechanics, 27 (2003b), pp. 767–790.
1354 34. Sheng D, Sloan SW, Yu HS. Aspects of finite element implementation of critical
1355   state models. Computational mechanics, 26 (2002), pp. 185–196.
1356 35. Sloan SW, Abbo AJ, Sheng D. Refined explicit integration of elastoplastic models
1357   with automatic error control. Engineering Computations, 18(1-2) (2001), pp. 121-
1358   154. Erratum: Engineering Computations, 19(5-6) (2002), pp. 594–594.
1359 36. Sloan SW. Substepping schemes for the numerical integration of elastoplastic stress-
1360   strain relations. International Journal for Numerical Methods in Engineering, 24
1361   (1987), pp. 893–911.
1362 37. Sołowski WT, Gallipoli D. Explicit stress integration with error control for the
1363   Barcelona Basic Model. Part I: Algorithms formulations. Computers and
1364   Geotechnics, 37(1-2) (2010a), pp. 59–67.

1365 38. Sołowski WT, Gallipoli D. Explicit stress integration with error control for the
1366   Barcelona Basic Model. Part II: Algorithms efficiency and accuracy. Computers and
1367   Geotechnics, 37(1-2) (2010b), pp. 68–81.

1368 39. Sołowski WT, Sloan SW. Elastic or Elasto-Plastic: Examination of Certain Strain
1369   Increments in the Barcelona Basic Model. Proc. 2nd Eur. conf. unsat. soils (eds C
1370   Mancuso, C Jommi, F D'Onza), Naples, (2012), Springer, pp. 85-91.

1371 40. Sołowski WT, Hofmann M, Hofstetter G, Sheng D, Sloan S. A comparative study
1372   of stress integration methods for the Barcelona Basic Model. Computers and
1373   Geotechnics, 44 (2012), pp. 22–33

1374 41. Tarantino A. A water retention model for deformable soils. Géotechnique, 59(9)
1375   (2009), pp. 751–762.

1376 42. Tsiampousi A, Zdravkovic L, Potts DM. Variation with time of the factor of safety
1377   of slopes excavated in unsaturated soils Computers and Geotechnics, 48(2) (2013),
1378   pp. 167–178.

1379 43. Wheeler SJ, Sharma RS, Buisson MSR. Coupling of hydraulic hysteresis and stress–
1380   strain behaviour in unsaturated soils. Géotechnique, 53(1) (2003), pp. 41–54.

1381 44. Zhao J, Sheng D, Rouainia M, Sloan SW. Explicit stress integration of complex soil
1382   models. International Journal for Numerical and Analytical Methods in
1383   Geomechanics, 29 (2005), pp. 1209–1229.

1384 45.45. Zhang Y, Zhou AN. Explicit integration of a porosity-dependent hydro-
1385   mechanical model for unsaturated soils. Int J Numer Anal Meth Geomech, 40
1386   (2016), pp. 2353-2382.

1387 46. Zhou AN, Sheng D. An advanced hydro-mechanical constitutive model for
1388   unsaturated soils with different initial densities. Computers and Geotechnics, 63
1389   (2015), pp. 44–66.